Noname manuscript No.
(will be inserted by the editor)

Bifurcation analysis of vortex induced vibration of low dimensional models of marine risers

Dan Wang · Zhifeng Hao · Ekaterina Pavlovskaia · Marian Wiercigroch

Received: date / Accepted: date

Abstract A low dimensional model of a top tensioned riser (TTR) under excitations from vortices and time-varying tension is proposed, where the van der Pol wake oscillator is used to simulate the loading caused by the vortex shedding. The governing partial differential equations describing the fluid-structure interactions are formulated and multi-mode approximations are obtained using the Galerkin projection method. The one mode approximation is applied in this study and two different resonances are investigated by employing the method of multiple scales. They are the 1:1 internal resonance between the structure and wake oscillator (also known as 'lock-in' phenomenon) and the combined 1:1 internal and 1:2 parametric resonances. Bifurcations under the varying nondimensional shedding frequency for different mass-damping parameters are investigated and the results of multiple scale analysis are compared with direct numerical simulations. Analytical responses are calculated using the continuation method and their stability is determined by examining the eigenvalues of the corresponding characteristic equations. Effects of the system parameters including the amplitude of the tension variation, vortex shedding frequency and mass-damping parameter on the system bifurcations have been investigated. The analytical approach has allowed to probe bifurcations occurring in the system and to identify stable and unstable responses. It is shown that the combined resonances can induce large-amplitude vibration of the structure. Counter intuitively, the amplitude of such responses increases rapidly as the amplitude of the tension variation grows. Comparisons between the analytical and numerical results confirm that the span of the system vibration can be accurately predicted analytically with respect to the obtained response amplitudes of responses. The proposed multi-mode approximation and presented findings of this study can be used to enhance design process of top tension risers.

Keywords Vortex-induced vibration · wake oscillator · parametric resonance · bifurcation diagram · marine riser model

Dan Wang · Zhifeng Hao
School of Mathematical Sciences, University of Jinan, Jinan 250022, China, E-mail: danwang2014518@hotmail.com, zhifenghao@hotmail.com

Ekaterina Pavlovskaia · Marian Wiercigroch
Centre for Applied Dynamics Research, School of Engineering, University of Aberdeen, King's College, Scotland, UK, E-mail: e.pavlovskaia@abdn.ac.uk, m.wiercigroch@abdn.ac.uk

1 Introduction

Long slender structures and their dynamic response characteristics have attracted significant fundamental and practical interests in the recent years. With the development of technology, risers have been used for oil and gas exploration and production in deep waters. The working conditions of risers are very complicated in deep waters, as sea waves and currents can occur simultaneously. Vortex-Induced Vibration (VIV) and parametric resonances are two main phenomena encountered in practice that can induce large-amplitude vibration of risers. Both phenomena have significant effect on the lifetime and safety of the structures but their mechanisms are still not entirely clear.

VIV phenomena arise from the interactions between the structures and fluid flow around them and forced and self-excited vibration are typically encountered. When the vortex shedding frequency approaches one of the natural frequency of the riser, the 'lock-in' phenomenon can occur, which if it is persistent may induce fatigue

damage of the structure. A number of comprehensive reviews [1–5] discuss earlier studies of VIV were focussed on the multi-mode response, VIV response at high Reynolds numbers, flow-induced vibrations between multiple marine risers, VIV of inclined risers and intermittent VIV in oscillatory flows, impacts of the floating platforms and internal flows, and other effects.

Experimental [6–11] (e.g. the full-scale, the small-scale, the model test) and numerical methods [12–19] (e.g. Finite Element, Computer Fluid Dynamics, force-decomposition, time-domain simulation methods) are used to analyse the dynamic responses of the risers. Effects of tensions on the in-line (IL) and cross-flow (CF) vibration amplitude and frequency responses, suppression of vibration, and hydrodynamic force coefficients were studied by Sanaati and Kato [20]. An experiment performed by Chen *et al.* [21] on the VIV of a flexible cable in an oncoming shear flow has shown that the cable model produced single-mode and multi-mode VIV under different oncoming velocities. They also found that amplitudes of displacement of the single mode VIV were larger than those of multi-mode VIV, and the cross-flow (CF) response was larger than that of in-line (IL) direction in both cases of single mode and multi-mode approximations. The flow-induced vibration (FIV) of an elastically mounted circular cylinder with different mass-damping parameters $m^*\zeta$ was studied in a wind channel by Hu *et al.* [22]. These results indicated that the vibration amplitude and region were gradually decreasing for the increasing values of $m^*\zeta$. In fact, effects of the mass-damping parameter $m^*\zeta$ on the responses of risers have been studied previously both using experimental models [23, 24] and test models [25, 26]. Effect of mass ratio on the vortex-induced vibrations of a top tensioned riser was investigated by Fu *et al.* [27] using a numerical method. An inverse method to obtain the hydrodynamic forces in the CF and IL directions of a flexible riser undergoing VIV based on measured strain was proposed by Song *et al.* [28]. A cylinder with low mass and damping was considered by Konstantinidis *et. al* [29], where an instantaneous phase between the cylinder motion and the fluid forcing was calculated.

The cost of the experimental and numerical analysis of the 3-D model of the risers coupled with a complex flows is high and often prohibitive. Hence some reduced order models were introduced to simulate the time-varying characteristics of fluid flow using wake oscillators such as the van der Pol oscillator, the Rayleigh oscillator, and others. The low-order models for the coupling between an elastically supported cylinder and wake oscillator were analysed by Facchinetti *et al.* [30], where displacement, velocity and acceleration couplings between the structure and the wake oscillator were introduced and analysed in detail. A semi-empirical theoretical model consisting of structural nonlinear equations of coupled motions in three directions (cross-flow, in-line and axial) for VIV was proposed in [31], in which the vortex-induced hydrodynamic lift and drag forces were simulated by two distributed and coupled wake oscillators. Due to the fact that wake oscillator models are semi-experimental, calibrations of fluid (namely coefficients of lift and drag force, mass-damping parameter, strength of nonlinear terms) are essential to explain the phenomena captured in the experiments. The calibrations and comparisons of the VIV of rigid cylinders on elastic supports were investigated by Postnikov *et al.* [32] and Kurushina *et al.* [33], and a similar approach was employed for flexible structures by Kurushina *et al.* [34]. Multi-modes responses of vortex-induced vibration of a slender pipe with two configurations were investigated by Pavlovskaia *et al.* [35], where the time varying lift force of vortices was modelled as the van der Pol oscillator. A new single wake oscillator with frequency dependent coupling for the model of VIV was proposed by Ogink and Metrikine [36], which was able to mimic observations from both the free and forced vibration experiments. Then the model was further improved as the nonlinear coupling wake oscillator by Qu and Metrikine [37].

The external excitation resulting from the time varying tension on the risers, especially for the top tensioned risers (TTRs) connecting the floating platform and the wellhead, can produce parametric resonances. TTRs can be subjected to the waves as well as currents in the real sea environments. Relative motions between the surface waves and floating platform can induce the fluctuations of the tension for the risers, which then can induce large-amplitude vibration of risers. Hsu [38] first analysed the marine cable parametric resonance in 1975. Some theoretical analyses at the early stage focussed on the nonlinear parametric responses of risers or tensioned cable legs. Nonlinear dynamic responses in the transverse direction of vertical marine risers or a tensioned cable legs subjected to parametric excitation at the top of the structure were studied by Chatjigeorgiou and Mavrakos [39], and results indicated that the transverse motion was dominated by the first mode of vibration, which was a subharmonic with respect to the parametric excitation. The 1:2 parametric excitation of a slender pipe conveying fluid for marine applications was analysed in [40], and the results indicated that under specific conditions, the dynamics of the structure in transverse direction can be described by the coupled Mathieu-Duffing oscillator.

With the development of technologies, impacts of the parametric excitation on the vibration of risers attract more and more attention as shown by the conducted experimental and numerical studies. The effect of top tension on dynamic behaviour of deep-sea risers was investigated numerically and experimentally by Zhang *et al.* [41], and results showed that the vibration displacement for TTR increases and the bending stress decreases as the top tension increases. The experiment of VIV for a vertical variable-tension riser was conducted by Li *et al.* [42], and it was shown that the dominant frequencies of risers in IL and CF directions, decrease gradually as the top tension is increased for a fixed flow velocity.

As experimental studies are expensive, various numerical simulations have been performed to analyse the dynamic responses of a TTR subjected to the varying tension during the VIV. Srinil [43] studied the VIV of the variable-tension vertical risers, and analysed effects of shear and tensioned-beam parameters (tension versus bending). Yang and Xiao [44] investigated the effects of the key design parameters on the dynamic properties of a TTR under the combined parametric and vortex-induced excitations. The parametric instability of a top-tensioned riser (TTR) in irregular waves was predicted for multi-frequency excitation in [45]. A coupled dynamic analysis of a marine riser under combined force excitation and parametric excitation was carried out by Yang *et al.* [46]. Results showed that responses of the first vibration mode were dominant under these two cases. Effects of tension variations on the VIV response were investigated in [47] by a numerical simulation, and results showed the VIV responses contain several modes and the dominating mode can vary with time. Numerical simulations of VIV for a vertical riser which is sinusoidally excited at its top end in both one and two directions in still water were carried out in [48]. Results revealed low-frequency oscillations at higher modes can be induced when the current speed varies along the span and the riser was excited at its top. The vibration amplitude of riser bending moment under combination action of sea currents and waves was bigger than that under sea current condition. Moreover, the riser total shear force has main relation with the first order mode under the sea current condition. A numerical method based on the force-decomposition model was proposed by Yuan *et al.* [49] to investigate the cross-flow VIV response characteristics with time-varying tension. A VIV dynamic model of a marine riser transporting fluid subjected to top harmonic tension in the cross flow was investigated in [50] by Finite Element Method. Results revealed that the excitation frequency of the harmonic tension near twice fundamental frequency of the riser had an important role in the displacement, and the displacements and stresses can increase as the harmonic tension amplitude increase. The study of horizontal parametric vibration of a compliant vertical access riser resulting from heave motion in the platform by Lou *et al.* [51] showed that the parametric excitation can occur mainly in first-order unstable regions. Mode coupling may have caused parametric excitation in the least stable regions. A parametrically excited top tensioned riser model subjected to simultaneous stochastic waves and vortex excitations was proposed in [52], and one of results showed more complicated and different dynamic responses can occur when the riser system is subjected to multi-frequency excitations. An improved time domain prediction model was proposed to simulate the riser subjected to axial parametric excitations by Gao *et al.* [53], and the numerical methods were used to study the responses for different cases. The results showed that vibration displacements of the riser were larger than those in the case without vessel heave motion. The stochastic response of a marine riser subjected to parametrical and external excitations was studied by Zhu *et al.* [54] with the path following method.

The cross-flow VIV response of a top tension riser under different flow fields was comprehensively studied in [55], where it was shown that the VIV responses of the riser exhibit obvious multi-modal characteristics.

In real life working conditions, risers can experience a combined vortex shedding and parametric excitation at the same time, which can has a significant impact on the safety and lifetime of risers. However, there are still many design challenges for top tensioned risers [56]. Studies on the combined resonances are limited, especially the theoretical study that would help to understand the mechanism of interactions between fluid and structure. In order to investigate the mechanisms of the combined resonances of risers, the reduced theoretical models of a TTR excited by the vortices and varying tension are proposed. The dynamic response characteristics are analysed for different values of mass-damping parameter.

The content of the paper is organized as follows. The mathematical models of a TTR under the combination of vortex shedding and parametric excitation are constructed in Section 2, where the wake oscillator is used to model the time-varying characteristic of the fluid flow. The first-mode equations of motion are derived by the Galerkin projection. In Section 3, the multiple scale method is used to analyse the dynamic system. The VIV phenomena and the combined vibration resulting from vortex shedding and parametric excitation, where dynamic responses computed analytically and verified by direct numerical simulation, are

studied in Section 4 and 5, respectively. Finally, the conclusions are drawn in Section 6.

2 Coupled model of structure and wake oscillator

The nonlinear models of a TTR under combined fluid flow and parametric tension variation excitation are presented in this section. Here, the wake oscillator approach is employed to simulate the time-varying characteristics of the vortex shedding. The partial differential equations of motion for fluid-structure interactions are derived and discretized using the Galerkin method. The reduced order coupled models of structure and wake oscillator are then obtained.

2.1 Model of structural vibration

The working conditions for a TTR are complex because currents and waves can occur simultaneously as shown schematically in Fig. 1(a), where the TTR is connected to a floating platform and a wellhead. Herein, a TTR is modeled as a uniform Euler-Bernoulli beam simply supported at both ends as presented in Fig. 1(b), where the top pre-tension $T_0 + \Delta T\cos(\omega_p t)$ varying harmonically is introduced. The pre-tension variation is chosen to avoid bottom tension becoming negative in this study. The current velocity U is assumed to be constant through the water column (along a riser), and only the transverse vibration of a riser in cross flow direction is considered.

The equation of motion for the transverse cross flow vibration of a uniform Euler-Bernoulli beam with varying tension can be presented as:

$$m_*\frac{\partial^2 w}{\partial t^2} + c\frac{\partial w}{\partial t} + \frac{\partial^2}{\partial z^2}\left(EI\frac{\partial^2 w}{\partial z^2}\right) - \frac{\partial}{\partial z}\left(T(z,t)\frac{\partial w}{\partial z}\right) = F_F(z,t), \tag{1}$$

where $w(z,t)$ is the cross flow transverse displacement, z is the axial position, $m_* = (\mu + C_a)\dfrac{\pi\rho_f D^2}{4}$ is the total mass per unit length including structural mass and added mass of fluid, μ is the mass ratio (which can affect on the range of 'lock-in' and the peak amplitude of the VIVs), C_a is the coefficient of fluid added mass, ρ_f is the density of the displaced fluid, D is the outer diameter of the riser, EI is the bending stiffness, c is the structural damping, and $F_F = F_D + F_L$ denotes the fluid force being calculated as a sum of fluid added damping and lift force due to the vortex-induced vibration. $T(z,t)$ is the varying axial tension which is calculated as

$$\begin{aligned} T(z,t) &= T_0 - (L-z)W_w + \Delta T\cos\omega_p t \\ &= T_b + W_w z + \Delta T\cos\omega_p t, \end{aligned}$$

where T_0 and T_b denote the top and bottom constant tension of the riser, $T_0 = T_b + LW_w$, W_w is the wet (apparent) weight of the riser per unit length, L is the length of the riser that is equal to the depth of water, ΔT is the amplitude of tension variation, and ω_p is the frequency of tension variation.

The lift fluid force acting on the structure are modelled as $F_L(t,z) = \dfrac{1}{2}\rho_f U^2 D C_L$, where C_L is the lift coefficient. In order to simulate the interactions between the structure and vortices, the time-varying variable $q = \dfrac{2C_L}{C_{L0}}$ is introduced [30,33,34,57–59], where C_{L0} is the reference lift coefficient. The lift force then can be written as

$$F_L(t,z) = \frac{1}{4}\rho_f U^2 D C_{L0} q.$$

The fluid added damping can be expressed as

$$F_D = -\frac{1}{2}C_D\rho_f D U\frac{\partial w}{\partial t},$$

where C_D is the coefficient of fluid added damping, U is the flow velocity. Therefore, the transverse cross flow vibration of the structure can be described by the following equation

$$\begin{aligned} m_*\frac{\partial^2 w}{\partial t^2} &+ c\frac{\partial w}{\partial t} + EI\frac{\partial^4 w}{\partial z^4} - W_w\frac{\partial w}{\partial z} \\ &- (T_b + W_w z + \Delta T\cos(\omega_p t))\frac{\partial^2 w}{\partial z^2} \\ &= -\frac{1}{2}C_D\rho_f D U\frac{\partial w}{\partial t} + \frac{1}{4}\rho_f U^2 D C_{L0} q. \end{aligned} \tag{2}$$

By introducing the following non-dimensional variables

$$v = \frac{w}{D}, \zeta = \frac{z}{L}, \tau = \omega_0 t,$$

and parameters

$$\Omega_f = 2\pi St\frac{U}{D}, \Omega_R = \frac{\Omega_f}{\omega_0}, \bar{\omega} = \frac{\omega_p}{\omega_0}, \xi = \frac{c}{2m_*\omega_0},$$

$$\beta = \frac{\Delta T}{T_b}, a = \frac{1}{4}\frac{C_D\rho_f D^2}{m_*}, b = \frac{\rho_f D^2 C_{L0}}{16 m_*}, r = \frac{W_w}{m_* L\omega_0^2},$$

Eq. (2) can be rewritten as

$$\begin{aligned} \frac{\partial^2 v}{\partial\tau^2} &+ 2\xi\frac{\partial v}{\partial\tau} + \frac{EI}{m_* L^4\omega_0^2}\frac{\partial^4 v}{\partial\zeta^4} - r\frac{\partial v}{\partial\zeta} \\ &- \frac{T_b}{m_* L^2\omega_0^2}(1+\beta\cos(\bar{\omega}\tau))\frac{\partial^2 v}{\partial\zeta^2} - r\zeta\frac{\partial^2 v}{\partial\zeta^2} \\ &= -\frac{1}{\pi St}a\Omega_R\frac{\partial v}{\partial\tau} + \frac{1}{\pi^2 St^2}b\Omega_R^2 q, \end{aligned} \tag{3}$$

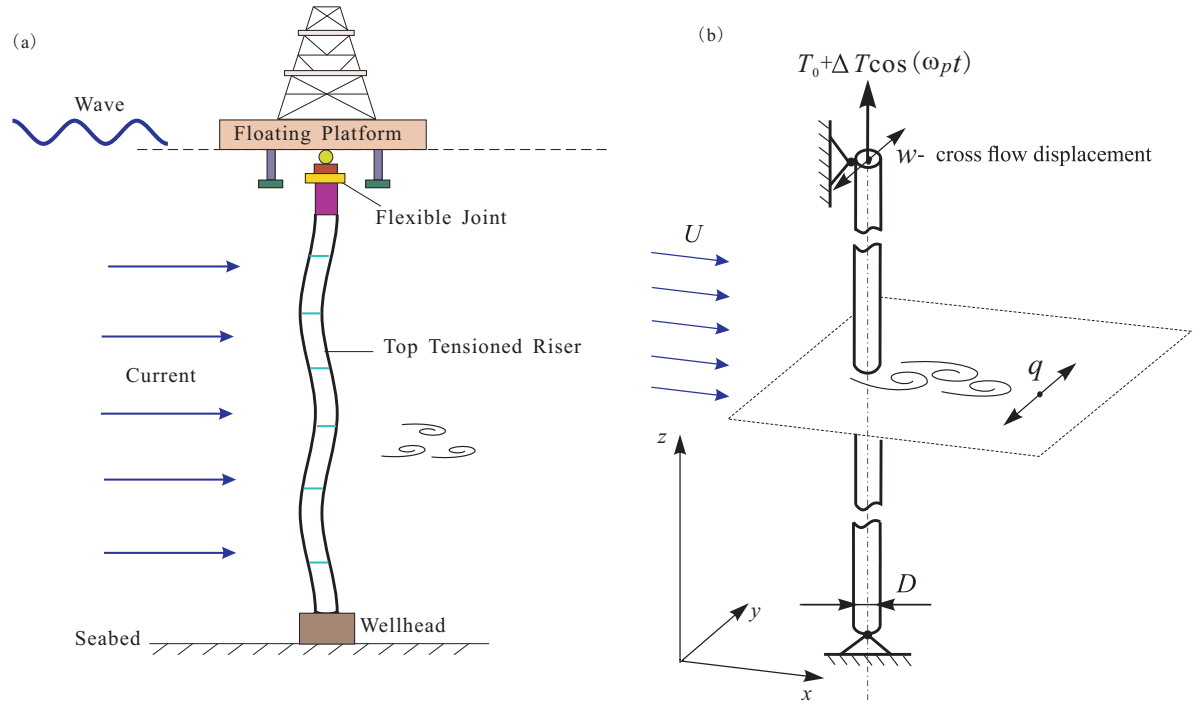

Fig. 1 (a) Schematic diagram of a TTR in the currents and waves: a TTR connected by the floating platform and wellhead; (b) physical model of the riser under excitation from the currents with velocity U and waves resulting in top varying tension.

where v is the nondimensional cross flow transverse displacement, ζ is the nondimensional axial position, ω_0 denotes the reference frequency, ξ is the damping ratio, Ω_f and Ω_R denote the shedding frequency and nondimensional shedding frequency of vortices, St is the Strouhal number, β and $\bar{\omega}$ are nondimensional amplitude and nondimensional frequency of the tension variation, and r is the wet weight ratio.

2.2 Wake oscillator model

The van der Pol oscillator is widely used to simulate the lift force acting on the structure [30,59–62], and the corresponding equation of the wake oscillator can be written as

$$\frac{\partial^2 q(t,z)}{\partial t^2} + \lambda\Omega_f\left(q^2(t,z)-1\right)\frac{\partial q(t,z)}{\partial t} + \Omega_f^2 q(t,z) = \frac{A}{D}\frac{\partial^2 w(t,z)}{\partial t^2}, \tag{4}$$

where λ is the van der Pol damping and A is the nondimensional coupling coefficient. Here the acceleration coupling is introduced as suggested in [30].

Similarly, Eq. (4) can be nondimensionalized as

$$\frac{\partial^2 q(\tau,\zeta)}{\partial \tau^2} + \lambda\Omega_R\left(q^2(\tau,\zeta)-1\right)\frac{\partial q(\tau,\zeta)}{\partial \tau} + \Omega_R^2 q(\tau,\zeta) = A\frac{\partial^2 v(\tau,\zeta)}{\partial \tau^2}. \tag{5}$$

2.3 Galerkin projection of the coupled system

Following earlier studies [33,61,62], an approximate solution of the Eqs (3) and (5) is obtained employing the Galerkin approach. Here the displacement and lift coefficient are assumed in the following form

$$v(\zeta,\tau) = \sum_{j=1}^{\infty} v_j(\tau)\tilde{v}_j(\zeta), \tag{6}$$

and

$$q(\zeta,\tau) = \sum_{j=1}^{\infty} q_j(\tau)\tilde{q}_j(\zeta), \tag{7}$$

where

$$\tilde{v}_j(\zeta) = \tilde{q}_j(\zeta) = \sin(j\pi\zeta). \tag{8}$$

Therefore

$$\int_0^1 \tilde{q}_j(\zeta)\tilde{q}_k(\zeta)d\zeta = \int_0^1 \tilde{v}_j(\zeta)\tilde{v}_k(\zeta)d\zeta = \begin{cases} 0, & j\neq k \\ \frac{1}{2}, & j=k \end{cases} \tag{9}$$

By substituting Eqs (6-8) into Eq. (3), multiplying it by $\tilde{v}_k(\zeta)$, integrating it along the length of the riser, and applying the orthogonality condition Eq. (9), we obtain

$$\ddot{v}_k(\tau) + 2\xi\dot{v}_k(\tau) + \frac{a\Omega_R}{\pi St}\dot{v}_k(\tau) + \left(\frac{EIk^4\pi^4}{m_* L^4\omega_0^2} + \frac{T_b k^2\pi^2}{m_* L^2\omega_0^2}(1+\beta\cos(\bar{\omega}\tau))\right)v_k(\tau) - 2r\sum_{j=1}^{\infty} j\pi v_j(\tau)\Phi_{jk} + 2r\sum_{j=1}^{\infty} v_j(\tau)j^2\pi^2\hat{\Phi}_{jk} = \frac{b\Omega_R^2}{\pi^2 St^2}q_k(\tau), \tag{10}$$

where dot denotes differentiation with respect to time τ, $\Phi_{jk} = \int_0^1 \cos(j\pi\zeta)\sin(k\pi\zeta)d\zeta$ and $\hat{\Phi}_{jk} = \int_0^1 \zeta\sin(j\pi\zeta)\sin(k\pi\zeta)d\zeta$.

Using the same approach Eq. (5) is transformed into the following equation

$$\ddot{q}_k(\tau) + 2\lambda\Omega_R\sum_{j=1}^{\infty}\sum_{m=1}^{\infty}\sum_{n=1}^{\infty} q_j(\tau)q_m(\tau)\dot{q}_n(\tau)\Psi_{jmnk} - \lambda\Omega_R\dot{q}_k(\tau) + \Omega_R^2 q_k(\tau) = A\ddot{v}_k(\tau), \tag{11}$$

where

$$\Psi_{jmnk} = \int_0^1 \sin(j\pi\zeta)\sin(m\pi\zeta)\sin(n\pi\zeta)\sin(k\pi\zeta)d\zeta.$$

According to previous studies [39–41], a parametric resonance often occurs at the low-order frequency of the structure. Therefore, in order to analyse the dynamics of the coupled system, the vibration of the first order modes for the riser and wake oscillator are investigated as follows.

When $k = j = 1$, $\Phi_{11} = 0$, $\hat{\Phi}_{11} = \frac{1}{4}$. By introducing $\omega_1 = \sqrt{\frac{EI\pi^4}{m_* L^4} + \frac{T_b\pi^2}{m_* L^2} + \frac{W_w\pi^2}{2m_* L}}$ (the natural frequency of the first-mode of the structure), $\omega_{R1} = \frac{\omega_1}{\omega_0}$, $\eta = \frac{T_b\pi^2}{m_* L^2\omega_0^2}$, $a = \frac{C_D}{\pi(\mu + C_a)}$ and $b = \frac{C_{L0}}{4\pi(\mu + C_a)}$, Eq. (10) becomes

$$\ddot{v}_1(\tau) + 2\xi\dot{v}_1(\tau) + \frac{a\Omega_R}{\pi St}\dot{v}_1(\tau) + \omega_{R1}^2 v_1(\tau) + \eta\beta\cos(\bar{\omega}\tau)v_1(\tau) = \frac{b\Omega_R^2}{\pi^2 St^2}q_1(\tau), \tag{12}$$

where ω_{R1} denotes the first nondimensional frequency of the structure and the reference frequency ω_0 is chosen as $\omega_0 = \omega_1$ in the following.

When $j = m = n = k = 1$, $\Psi_{1111} = \frac{3}{8}$ and the vibration of the first mode equation for the van der Pol oscillator can be obtained as

$$\ddot{q}_1(\tau) + \lambda\Omega_R\left(\frac{3}{4}q_1^2(\tau) - 1\right)\dot{q}_1(\tau) + \Omega_R^2 q_1(\tau) = A\ddot{v}_1(\tau). \tag{13}$$

Eqs (12) and (13) are one mode approximation of the model describing the interactions between the fluid flows and structure. Although the analysis presented in this paper is only conducted for this approximation, the overall procedure of Galerkin discretization described here allows to obtain the higher mode approximations. The subscripts of v_1 and q_1 are omitted in the following analysis, where variables v and q are used instead to simplify derivations.

3 Application of multiple scale method

In this nonlinear system which is similar to the Mathieu–van der Pol type oscillators, a rich dynamic behaviour can occur, especially under the resonance conditions. In order to investigate the qualitative features of the system, the multiple scale method [59,63] is used to analyse possible resonances.

By introducing the scaled parameters as $C_D \to \varepsilon\tilde{C}_D$ (indicating $a \to \varepsilon\tilde{a}$), $C_{L0} \to \varepsilon\tilde{C}_{L0}$ (indicating $b \to \varepsilon\tilde{b}$), $\lambda \to \varepsilon\tilde{\lambda}$, $A \to \varepsilon\tilde{A}$, $\beta \to \varepsilon\tilde{\beta}$, $\xi \to \varepsilon\tilde{\xi}$, Eqs (12) and (13) can be expressed as

$$\ddot{v} + \omega_{R1}^2 v = \frac{\varepsilon\tilde{b}\Omega_R^2}{\pi^2 St^2}q - \varepsilon\left(2\tilde{\xi} + \frac{\tilde{a}\Omega_R}{\pi St}\right)\dot{v} - \varepsilon\eta\tilde{\beta}\cos(\bar{\omega}\tau)v, \tag{14}$$

$$\ddot{q} + \Omega_R^2 q = \varepsilon\tilde{A}\ddot{v} - \varepsilon\tilde{\lambda}\Omega_R\left(\frac{3}{4}q^2 - 1\right)\dot{q}. \tag{15}$$

To construct approximate solutions, the method of multiple scales in employed in this study assuming two time scales T_0 and T_1 ($T_n = \varepsilon^n\tau, n = 0, 1$) so that

$$\begin{aligned} v(\tau) &= v_0(T_0, T_1) + \varepsilon v_1(T_0, T_1), \\ q(\tau) &= q_0(T_0, T_1) + \varepsilon q_1(T_0, T_1). \end{aligned} \tag{16}$$

Here only first order terms are retained so derivatives with respect to time τ can be expressed as $\frac{\mathrm{d}}{\mathrm{d}\tau} = D_0 + \varepsilon D_1$, $\frac{\mathrm{d}^2}{\mathrm{d}\tau^2} = D_0^2 + 2\varepsilon D_0 D_1$, $D_n = \frac{\partial}{\partial T_n}(n = 0, 1)$ and $D_0^2 = \frac{\partial^2}{\partial T_0^2}$.

Substituting (16) into Eqs (14) and (15), and collecting terms in powers of ε, one can obtain that:

ε^0 :

$$D_0^2 v_0 + \omega_{R1}^2 v_0 = 0, \tag{17}$$

$$D_0^2 q_0 + \Omega_R^2 q_0 = 0. \tag{18}$$

ε^1:

$$D_0^2 v_1 + \omega_{R1}^2 v_1 = -\left(2\tilde{\xi} + \frac{\tilde{a}\Omega_R}{\pi St}\right)D_0 v_0 - 2D_0 D_1 v_0 + \frac{\tilde{b}\Omega_R^2 q_0}{\pi^2 St^2} - \eta\tilde{\beta}\frac{e^{i\bar{\omega}\tau} + e^{-i\bar{\omega}\tau}}{2}v_0, \tag{19}$$

$$D_0^2 q_1 + \Omega_R^2 q_1 = \tilde{A}D_0^2 v_0 - 2D_0 D_1 q_0 - \tilde{\lambda}\Omega_R\left(\frac{3}{4}q_0^2 - 1\right)D_0 q_0, \tag{20}$$

where $\cos(\bar{\omega}\tau)$ from Eq. (14) is expressed in the complex form in Eq. (19) and i denotes the imaginary number.

The solutions of Eqs (17) and (18) can be expressed as

$$v_0 = V(T_1)e^{i\omega_{R1}T_0} + \bar{V}(T_1)e^{-i\omega_{R1}T_0}, \tag{21}$$

$$q_0 = Q(T_1)e^{i\Omega_R T_0} + \bar{Q}(T_1)e^{-i\Omega_R T_0}, \tag{22}$$

where $\bar{V}$ and $\bar{Q}$ denote the complex conjugates of functions V, Q, which can be expressed in the complex form as

$$V = \frac{1}{2}a_1(T_1)e^{i\theta_1(T_1)}, \tag{23}$$

$$Q = \frac{1}{2}a_2(T_1)e^{i\theta_2(T_1)}, \tag{24}$$

and a_j, θ_j (j=1, 2) denote the amplitudes and phase angles, respectively.

Substituting the anticipated solutions (21) and (22) into Eqs (19) and (20), we obtain

$$\begin{aligned}
D_0^2 v_1 + \omega_{R1}^2 v_1 = & -i\omega_{R1}\left(2\tilde{\xi} + \frac{\tilde{a}\Omega_R}{\pi St}\right)Ve^{i\omega_{R1}T_0} \\
& - 2i\omega_{R1}D_1 Ve^{i\omega_{R1}T_0} + \frac{\tilde{b}\Omega_R^2}{\pi^2 St^2}Qe^{i\Omega_R T_0} \\
& - \frac{1}{2}\eta\tilde{\beta}V[e^{i(\bar{\omega}+\omega_{R1})T_0} + e^{i(\omega_{R1}-\bar{\omega})T_0}] \\
& + i\omega_{R1}\left(2\tilde{\xi} + \frac{\tilde{a}\Omega_R}{\pi St}\right)\bar{V}e^{-i\omega_{R1}T_0} \\
& + 2i\omega_{R1}D_1\bar{V}e^{-i\omega_{R1}T_0} + \frac{\tilde{b}\Omega_R^2}{\pi^2 St^2}\bar{Q}e^{-i\Omega_R T_0} \\
& - \frac{1}{2}\eta\tilde{\beta}\bar{V}[e^{-i(\bar{\omega}+\omega_{R1})T_0} + e^{-i(\omega_{R1}-\bar{\omega})T_0}],
\end{aligned} \tag{25}$$

$$\begin{aligned}
D_0^2 q_1 + \Omega_R^2 q_1 = & -\omega_{R1}^2\tilde{A}e^{i\omega_{R1}T_0}V - 2i\Omega_R e^{i\Omega_R T_0}D_1 Q \\
& - i\tilde{\lambda}\Omega_R^2\left[\frac{3}{4}Q^3 e^{3i\Omega_R T_0} + \left(\frac{3}{4}Q\bar{Q} - 1\right)Qe^{i\Omega_R T_0}\right] \\
& + i\tilde{\lambda}\Omega_R^2\left[\frac{3}{4}\bar{Q}^3 e^{-3i\Omega_R T_0} + \left(\frac{3}{4}Q\bar{Q} - 1\right)\bar{Q}e^{-i\Omega_R T_0}\right] \\
& - \omega_{R1}^2\tilde{A}e^{-i\omega_{R1}T_0}\bar{V} + 2i\Omega_R e^{-i\Omega_R T_0}D_1\bar{Q}.
\end{aligned} \tag{26}$$

Eqs (25) and (26) indicate possible resonances between the frequencies Ω_R, ω_{R1} and $\bar{\omega}$. Two types of resonances are investigated in the current study. First case is the 1:1 internal resonance between the frequencies Ω_R and ω_{R1}, and the other case is the combined resonance including the internal resonance and parametric resonance.

4 Internal resonance for the VIV

In riser systems, an important 'lock-in' phenomenon is observed when the frequency of the vortex shedding is close to a natural frequency of the riser. Therefore, the internal resonance between the structure and wake oscillator is investigated first. Here the frequency-amplitude response and bifurcation curves are derived, hence the effects of parameters can be studied.

4.1 Solvability conditions

First of all we assume that nondimensional frequencies of wake oscillator and structure are related as $\Omega_R = \omega_{R1} + \varepsilon\sigma$, where σ is the detuning parameter. Then taking into account that $T_1 = \varepsilon T_0$, the secular terms can be eliminated by satisfying the solvability conditions. Here, complex conjugate terms do not appear as they are automatically eliminated if the conditions below are fulfilled [64],

$$\begin{aligned}
& - i\omega_{R1}\left(2\tilde{\xi} + \frac{\tilde{a}\Omega_R}{\pi St}\right)V - 2i\omega_{R1}D_1 V \\
& + \frac{\tilde{b}\Omega_R^2}{\pi^2 St^2}Qe^{i\sigma T_1} = 0,
\end{aligned} \tag{27}$$

$$\begin{aligned}
& - \omega_{R1}^2\tilde{A}e^{-i\sigma T_1}V - 2i\Omega_R D_1 Q \\
& - i\tilde{\lambda}\Omega_R^2\left(\frac{3}{4}Q\bar{Q} - 1\right)Q = 0.
\end{aligned} \tag{28}$$

The derivatives of amplitudes V and Q with respect to T_1 can be obtained as

$$D_1 V = -\left(\tilde{\xi} + \frac{\tilde{a}\Omega_R}{2\pi St}\right)V - \frac{i\tilde{b}\Omega_R^2}{2\omega_{R1}\pi^2 St^2}Qe^{i\sigma T_1}, \tag{29}$$

$$D_1 Q = \frac{1}{2}\frac{\omega_{R1}^2}{\Omega_R}i\tilde{A}e^{-i\sigma T_1}V - \frac{1}{2}\tilde{\lambda}\Omega_R\left(\frac{3}{4}Q\bar{Q} - 1\right)Q. \tag{30}$$

By substituting (23) and (24) into Eqs (29) and (30), the first-order differential equations can be obtained after separating the real and imaginary parts:

$$a_1{}' = -\left(\tilde{\xi} + \frac{\tilde{a}\Omega_R}{2\pi St}\right)a_1 + \frac{\tilde{b}\Omega_R^2 a_2}{2\omega_{R1}\pi^2 St^2}\sin\Phi, \tag{31}$$

$$\theta_1{}' = -\frac{\tilde{b}\Omega_R^2 a_2}{2\omega_{R1}\pi^2 St^2 a_1}\cos\Phi, \tag{32}$$

$$a_2{}' = \frac{1}{2}\frac{\omega_{R1}^2\tilde{A}a_1}{\Omega_R}\sin\Phi - \frac{1}{2}\tilde{\lambda}\Omega_R a_2\left(\frac{3}{16}a_2^2 - 1\right), \tag{33}$$

$$\theta_2{}' = \frac{1}{2}\frac{\omega_{R1}^2}{\Omega_R a_2}\tilde{A}a_1\cos\Phi. \tag{34}$$

where $\Phi = \theta_2 + \sigma T_1 - \theta_1$ and $'$ denotes derivative with respect to T_1. The first-order differential equation of Φ can be derived from Eqs (32) and (34) as

$$\Phi' = \sigma + \frac{1}{2}\frac{\omega_{R1}^2}{\Omega_R a_2}\tilde{A}a_1\cos\Phi + \frac{\tilde{b}\Omega_R^2 a_2}{2\omega_{R1}\pi^2 St^2 a_1}\cos\Phi. \tag{35}$$

The steady-state solutions can be obtained when letting $a_j{}' = 0$ (j=1, 2), $\Phi' = 0$ in Eqs (31), (33) and (35). Then eliminating variable Φ from the obtained equations and using standard equality $\cos^2\Phi + \sin^2\Phi =$

1, the following equations for unknown amplitude a_1 and a_2 are derived:

$$F_1(a_1,a_2)=2\tilde{A}\omega_{R1}^3\pi^2St^2\left(\tilde{\xi}+\frac{\tilde{a}\Omega_R}{2\pi St}\right)a_1^2$$
$$-\tilde{b}\tilde{\lambda}\Omega_R^4a_2^2\left(\frac{3}{16}a_2^2-1\right)=0,$$
$$F_2(a_1,a_2)=a_1^2a_2^2\left[\tilde{\xi}+\frac{\tilde{a}\Omega_R}{2\pi St}+\frac{1}{2}\tilde{\lambda}\Omega_R\left(\frac{3}{16}a_2^2-1\right)\right]^2$$
$$+\sigma^2a_1^2a_2^2-\left(\frac{1}{2}\frac{\omega_{R1}^2}{\Omega_R}\tilde{A}a_1^2+\frac{\tilde{b}\Omega_R^2a_2^2}{2\omega_{R1}\pi^2St^2}\right)^2=0.$$

These two equations can be rewritten as scaled parameters change back to the original ones, namely

$$2A\omega_{R1}^3\pi^2St^2\left(\xi+\frac{a\Omega_R}{2\pi St}\right)a_1^2-$$
$$b\lambda\Omega_R^4a_2^2\left(\frac{3}{16}a_2^2-1\right)=0, \tag{36}$$
$$a_1^2a_2^2\left[\xi+\frac{a\Omega_R}{2\pi St}+\frac{1}{2}\lambda\Omega_R\left(\frac{3}{16}a_2^2-1\right)\right]^2+$$
$$(\Omega_R-\omega_{R1})^2a_1^2a_2^2-$$
$$\left(\frac{1}{2}\frac{\omega_{R1}^2}{\Omega_R}Aa_1^2+\frac{b\Omega_R^2a_2^2}{2\omega_{R1}\pi^2St^2}\right)^2=0. \tag{37}$$

Eqs (36) and (37) can be solved numerically to find steady-state amplitudes.

The first-order equations of v_1 and q_1 can be simplified to

$$D_0^2v_1+\omega_{R1}^2v_1=-\frac{\eta\tilde{\beta}}{4}a_1[e^{i((\bar{\omega}+\omega_{R1})T_0+\theta_1)}$$
$$+e^{i((\omega_{R1}-\bar{\omega})T_0+\theta_1)}]$$
$$-\frac{\eta\tilde{\beta}}{4}a_1[e^{-i((\bar{\omega}+\omega_{R1})T_0+\theta_1)}+e^{-i((\omega_{R1}-\bar{\omega})T_0+\theta_1)}]. \tag{38}$$
$$D_0^2q_1+\Omega_R^2q_1=-\frac{3}{32}i\tilde{\lambda}\Omega_R^2a_2^3e^{3i(\Omega_RT_0+\theta_2)}$$
$$+\frac{3}{32}i\tilde{\lambda}\Omega_R^2a_2^3e^{-3i(\Omega_RT_0+\theta_2)}. \tag{39}$$

Solutions of v_1 and q_1 can be obtained from Eqs (38) and (39) as

$$v_1=-\frac{\eta\tilde{\beta}a_1[e^{i((\bar{\omega}+\omega_{R1})T_0+\theta_1)}+e^{-i((\bar{\omega}+\omega_{R1})T_0+\theta_1)}]}{4[\omega_{R1}^2-(\bar{\omega}+\omega_{R1})^2]}$$
$$-\frac{\eta\tilde{\beta}a_1[e^{i((\omega_{R1}-\bar{\omega})T_0+\theta_1)}+e^{-i((\omega_{R1}-\bar{\omega})T_0+\theta_1)}]}{4[\omega_{R1}^2-(\omega_{R1}-\bar{\omega})^2]}, \tag{40}$$

$$q_1=\frac{3i\tilde{\lambda}a_2^3}{256}e^{3i(\Omega_RT_0+\theta_2)}-\frac{3i\tilde{\lambda}a_2^3}{256}e^{-3i(\Omega_RT_0+\theta_2)}. \tag{41}$$

Thus the first order approximate solutions of v and q can be obtained by combining the solutions for (v_0, q_0) and (v_1, q_1)

$$v\approx v_0+\varepsilon v_1=a_1\cos(\omega_{R1}T_0+\theta_1)$$
$$-\frac{\varepsilon\eta\tilde{\beta}a_1}{2}\left[\frac{\cos((\bar{\omega}+\omega_{R1})T_0+\theta_1)}{\omega_{R1}^2-(\bar{\omega}+\omega_{R1})^2}\right.$$
$$\left.+\frac{\cos((\omega_{R1}-\bar{\omega})T_0+\theta_1)}{\omega_{R1}^2-(\omega_{R1}-\bar{\omega})^2}\right], \tag{42}$$

$$q\approx q_0+\varepsilon q_1=a_2\cos(\Omega_RT_0+\theta_2)$$
$$-\frac{3\varepsilon\tilde{\lambda}a_2^3}{128}\sin(3(\Omega_RT_0+\theta_2)), \tag{43}$$

where the amplitudes a_1 and a_2 satisfy Eqs (36) and (37). As can be seen from Eq. (42), that the parametric excitation only affects the first order solution v_1, and also a weak effect on the approximation of v. Correspondingly, this has no obvious influence on the dynamic response q, representing the van der Pol oscillator.

4.2 Amplitude–frequency curves

As can be seen from Eqs (36) and (37), $a_1 = 0$ and $a_2 = 0$ are the trivial solutions giving zero amplitude responses. Other solutions can be obtained numerically using the method presented in [64], and therefore amplitude-frequency curves can be computed where the stabilities are determined by examining the eigenvalues of the corresponding characteristic equations [65] for the dynamical system described by Eqs (31), (33) and (35).

In order to investigate effects of the added mass coefficient μ and nondimensional damping coefficient ξ, four sets of system parameters shown in Table 1 are chosen to calculate the amplitude–frequency curves. The other parameters are fixed as $C_D = 2, C_{L0} = 0.3, C_a = 1, \lambda = 0.3, A = 12, St = 0.2$ [30,33,62].

Figure 2 shows the analytical results obtained from Eqs (36) and (37) as solid curves and the results from a direct numerical integration of Eqs (12) and (13), where the obtained maximum values of the displacements for each selected Ω_R are presented by circles under different mass-damping parameters. The other parameters are fixed at $\eta = 0.8, \beta = 0.001, \bar{\omega} = 0.2, \omega_{R1} = 1$. As can be seen from Fig. 2, when increasing the nondimensional shedding frequency Ω_R, the amplitudes a_1 and a_2 increase slowly at first to $\Omega_R \approx 0.5$, and then grow rapidly to the maximum values near the resonance frequency $\Omega_R \approx 1$. As Ω_R is increased further, the amplitudes a_1 and a_2 decrease rapidly at first to $\Omega_R \approx 1.5$ and then continue to gradually decrease. It should be noted that the amplitude of vibration of the structure and wake oscillator at the resonance is smaller for larger values of

Table 1 Selected structural parameters with different mass ratios and damping ratios chosen from the previous studies

	mass ratio μ	damping ratio ξ	mass-damping parameter $\mu\xi$
Sun's riser model (2014) [26]	1	0.003	0.0030
Tsahalis and Jones (1981) [23]	2.45	0.00796	0.0195
Yang et al.(2009)[24]	3.87	0.0152	0.0588
He's riser model(2010)[25]	2.9	0.045	0.1305

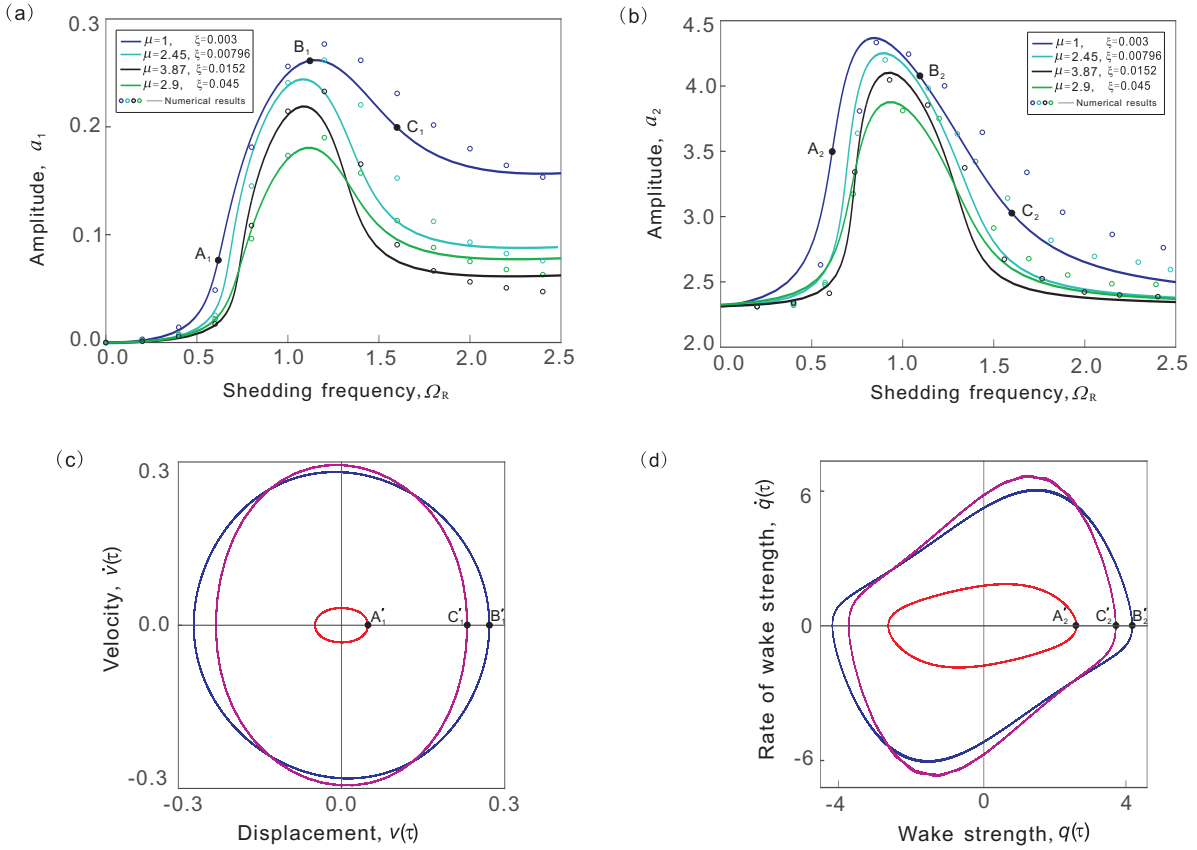

Fig. 2 Dynamic responses amplitudes for (a) the structure and (b) the wake oscillator as function of the nondimensional shedding frequency Ω_R obtained analytically (marked by solid curves) and numerically (marked by circles) for different values of mass-damping parameters and for fixed other parameters as $\eta = 0.8, \beta = 0.001, \bar{\omega} = 0.2$ and $\omega_{R1} = 1$. (c) and (d) show phase portraits for the structure and the wake oscillator calculated using Eqs (12) and (13) for $\mu = 1, \xi = 0.003$ and $\Omega_R = 0.6$ (red), 1.1 (blue) and 1.6 (purple).

the mass-damping parameter. This is illustrated in Figs 2(a) and 2(b) by points $A_1(0.6, 0.0645)$, $B_1(1.1, 0.2606)$, $C_1(1.6, 0.1993)$ and $A_2(0.6, 3.3851)$, $B_2(1.1, 4.0621)$, $C_2(1.6, 3.0247)$, are marked with the black solid circles.

Figs 2(c) and 2(d) present the phase portraits of system computed numerically using Eqs (12) and (13) for $\mu = 1, \xi = 0.003$ at $\Omega_R = 0.6, 1.1$ and 1.6. The abscissa of the points A_i', B_i', and C_i', $(i = 1, 2)$, are the maximum amplitude of responses of the structure and van der Pol oscillator computed for $\Omega_R = 0.6$, 1.1 and 1.6 respectively.The other parameters $A_1'(0.0594, 0)$, $B_1'(0.2709, 0)$, $C_1' = (0.2309, 0)$ and $A_2' = (2.7645, 0)$, $B_2' = (4.1665, 0)$, $C_2' = (3.7214, 0)$, show the evolution of the amplitudes on phase planes (panels (c) and (d) of Fig. 2) used to construct the frequency-amplitude curved (panels (a) and (b) of Fig. 2). Although the presented comparison demonstrates some differences between the analytical and numerical results, which are more evident for the frequencies above the resonance, the presented approach allows to determine the overall shape of the resonance curves and the maximum values of the displacement amplitudes reasonably well.

5 Combined resonances of the TTR

As can be seen from Eqs (31)-(34), the parametric excitation contributes to the system responses in the first order approximate solution $v_1(\tau)$. However, the parametric resonance can induce large vibration of the structure. In order to understand this phenomenon more clearly, the internal resonance coupled with the parametric resonance is investigated in this section. The frequency-amplitude response equations and bifurcation curves are constructed and then the effects of parameters on the system responses are studied.

5.1 Solvability conditions

We assume that the following relations between the frequencies are satisfed $\Omega_R = \omega_{R1} + \varepsilon\sigma_1$, $\bar{\omega} = 2\omega_{R1} + \varepsilon\sigma_2$, where σ_1 and σ_2 are the detuning parameters. Then the solvability conditions can be obtained from Eqs (25) and (26) in the same way as before,

$$
\begin{aligned}
&-i\omega_{R1}\left(2\tilde{\xi}+\frac{\tilde{a}\Omega_R}{\pi St}\right)V-2i\omega_{R1}D_1V\\
&+\frac{\tilde{b}\Omega_R^2}{\pi^2St^2}Qe^{i\sigma_1T_1}-\frac{\eta\tilde{\beta}}{2}\bar{V}e^{i\sigma_2T_1}=0, \qquad (44)\\
&-\omega_{R1}^2\tilde{A}e^{-i\sigma_1T_1}V-2i\Omega_RD_1Q\\
&-i\tilde{\lambda}\Omega_R^2\left(\frac{3}{4}Q\bar{Q}-1\right)Q=0. \qquad (45)
\end{aligned}
$$

By re-arranging these equations, one can obtain

$$
\begin{aligned}
D_1V=&-\left(\tilde{\xi}+\frac{\tilde{a}\Omega_R}{2\pi St}\right)V-\frac{i\tilde{b}\Omega_R^2}{2\omega_{R1}\pi^2St^2}Qe^{i\sigma_1T_1}\\
&+\frac{i\eta\tilde{\beta}}{4\omega_{R1}}\bar{V}e^{i\sigma_2T_1}, \qquad (46)\\
D_1Q=&\frac{1}{2}\frac{\omega_{R1}^2}{\Omega_R}i\tilde{A}Ve^{-i\sigma_1T_1}-\frac{1}{2}\tilde{\lambda}\Omega_R\left(\frac{3}{4}Q\bar{Q}-1\right)Q. \qquad (47)
\end{aligned}
$$

Here functions V and Q can also be expressed as before by Eqs (23) and (24) where the unknown amplitudes a_1 and a_2 will now satisfy new set of the equations (Eqs (54) and (55)) derived later in this section. Substituting the complex variable expressions of Eqs (23) and (24) into Eqs (46) and (47), the first-order differential equations can be obtained after separating the real and imaginary parts as

$$
\begin{aligned}
{a_1}'=&-\left(\tilde{\xi}+\frac{\tilde{a}\Omega}{2\pi St}\right)a_1+\frac{\tilde{b}\Omega_R^2a_2}{2\omega_{R1}\pi^2St^2}\sin\Phi_1\\
&-\frac{\eta\tilde{\beta}a_1}{4\omega_{R1}}\sin\Phi_2, \qquad (48)\\
{\theta_1}'=&-\frac{\tilde{b}\Omega_R^2a_2}{2\omega_{R1}\pi^2St^2a_1}\cos\Phi_1+\frac{\eta\tilde{\beta}}{4\omega}\cos\Phi_2, \qquad (49)
\end{aligned}
$$

$$
a_2'=\frac{1}{2}\frac{\omega_{R1}^2}{\Omega_R}\tilde{A}a_1\sin\Phi_1-\frac{1}{2}\tilde{\lambda}\Omega_Ra_2\left(\frac{3}{16}a_2^2-1\right), \qquad (50)
$$

$$
\theta_2'=\frac{1}{2}\frac{\omega_{R1}^2}{\Omega_Ra_2}\tilde{A}a_1\cos\Phi_1, \qquad (51)
$$

where $\Phi_1=\theta_2+\sigma_1T_1-\theta_1, \Phi_2=\sigma_2T_1-2\theta_1$.

Furthermore, the first order differential equation of Φ_1 and Φ_2 with respect to time T_1 can be derived from Eqs (49) and (51) as

$$
\begin{aligned}
{\Phi'}_1=&\sigma_1+\frac{1}{2}\frac{\omega_{R1}^2}{\Omega_Ra_2}\tilde{A}a_1\cos\Phi_1\\
&+\frac{\tilde{b}\Omega_R^2a_2}{2\omega_{R1}\pi^2St^2a_1}\cos\Phi_1-\frac{\eta\tilde{\beta}}{4\omega}\cos\Phi_2, \qquad (52)\\
{\Phi'}_2=&\sigma_2+\frac{\tilde{b}\Omega_R^2a_2}{\omega_{R1}\pi^2St^2a_1}\cos\Phi_1-\frac{\eta\tilde{\beta}}{2\omega_{R1}}\cos\Phi_2. \qquad (53)
\end{aligned}
$$

The steady-state solutions can be obtained assuming ${a_1}'=0, {a_2}'=0, \Phi_1'=0, \Phi_2'=0$ as follows

$$
\begin{aligned}
&G_1(a_1,a_2)=\\
&\left[\frac{\tilde{b}\tilde{\lambda}\Omega_R^4a_2^2}{\omega_{R1}^3\pi^2St^2\tilde{A}}\left(\frac{3}{16}a_2^2-1\right)-a_1^2\left(2\tilde{\xi}+\frac{\tilde{a}\Omega_R}{\pi St}\right)\right]^2\\
&+\left[a_1^2\sigma_2+\frac{\tilde{b}\Omega_R^3(\sigma_2-2\sigma_1)a_2^2}{\omega_{R1}^3\pi^2St^2\tilde{A}}\right]^2-\frac{\eta^2\tilde{\beta}^2}{4\omega_{R1}^2}a_1^4=0,\\
&G_2(a_1,a_2)=\tilde{\lambda}^2\Omega_R^2a_2^2\left(\frac{3}{16}a_2^2-1\right)^2\\
&+(\sigma_2-2\sigma_1)^2a_2^2-\frac{\omega_{R1}^4}{\Omega_R^2}\tilde{A}^2a_1^2=0.
\end{aligned}
$$

The above equations are rewritten as the scaled parameters change back to the original ones as follows.

$$
\begin{aligned}
&\left[\frac{b\lambda\Omega_R^4a_2^2}{\omega_{R1}^3\pi^2St^2A}\left(\frac{3}{16}a_2^2-1\right)-a_1^2\left(2\xi+\frac{a\Omega_R}{\pi St}\right)\right]^2\\
&+\left[a_1^2(\bar{\omega}-2\omega_{R1})+\frac{b\Omega_R^3(\bar{\omega}-2\Omega_R)a_2^2}{\omega_{R1}^3\pi^2St^2A}\right]^2\\
&-\frac{\eta^2\beta^2}{4\omega_{R1}^2}a_1^4=0, \qquad (54)\\
&\lambda^2\Omega_R^2a_2^2\left(\frac{3}{16}a_2^2-1\right)^2+(\bar{\omega}-2\Omega_R)^2a_2^2\\
&-\frac{\omega_{R1}^4}{\Omega_R^2}A^2a_1^2=0. \qquad (55)
\end{aligned}
$$

In order to analyse the effects of the nondimensional shedding frequency Ω_R on the responses, Eqs (54) and (55) are solved numerically. It should be noted that as before these equations have trivial solutions $a_1=0$ and $a_2=0$.

Similarly, the first order solutions of v_1 and q_1 can be obtained as

$$v_1 = -\frac{\eta\tilde{\beta}a_1[e^{i((\bar{\omega}+\omega_{R1})T_0+\theta_1)} + e^{-i((\bar{\omega}+\omega_{R1})T_0+\theta_1)}]}{4[\omega_{R1}^2 - (\bar{\omega}+\omega_{R1})^2]},$$
$$q_1 = \frac{3i\tilde{\lambda}a_2^3[e^{3i(\Omega_R T_0+\theta_2)} - e^{-3i(\Omega_R T_0+\theta_2)}]}{256}.$$

Thus the first order approximate solutions of v and q can be obtained by combining solutions (v_0, q_0) and (v_1, q_1)

$$v \approx v_0 + \varepsilon v_1 = a_1\cos(\omega_{R1}T_0+\theta_1) - \frac{\varepsilon\eta\tilde{\beta}a_1}{2}\frac{\cos((\bar{\omega}+\omega_{R1})T_0+\theta_1)}{\omega_{R1}^2 - (\bar{\omega}+\omega_{R1})^2},$$

$$q \approx q_0 + \varepsilon q_1 = a_2\cos(\Omega_R T_0+\theta_2) - \frac{3\varepsilon\tilde{\lambda}a_2^3\sin(3(\Omega_R T_0+\theta_2))}{128},$$

where amplitudes a_1 and a_2 can be found from Eqs (54) and (55).

5.2 Analysis of the amplitude-frequency curves

Non-trivial solutions of Eqs (54) and (55) provide the amplitudes of the vibration responses of the structure and the wake oscillator as functions of the nondimensional shedding frequency Ω_R, and they are obtained in this study by using the parameter continuation method. In order to analyse the influence of the parametric force on the system responses, different values in a large range of the amplitude ratio β are considered and bifurcation curves are computed under the resonance condition. Their stabilities are determined by examining the eigenvalues of the corresponding characteristic equations for (48), (50), (52) and (53). The numerical bifurcation curves are also calculated by using the Runge-Kutta method to verify the analytical results. The fixed parameters are chosen at $C_D = 2, C_{L0} = 0.3, C_a = 1, \lambda = 0.3, A = 12, St = 0.2, \eta = 0.8, \omega_{R1} = 1$ and $\bar{\omega} = 2.1$, respectively.

Figure 3 presents bifurcation curves of the dynamic responses of the structure computed for 4 different values of the amplitude ratio β at $\mu = 1, \xi = 0.003$. Here only structural response $a_1(\Omega_R)$ is shown as the wake oscillator response $a_2(\Omega_R)$ has the same behaviour. As can be seen from Fig. 3(a) obtained for $\beta = 0.8$, only trivial solution exists below $\Omega_R \approx 0.4216$ where an unstable non-trivial solution is born via the Hopf bifurcation (labeled by letter H). As the frequency increases, amplitude of this unstable solution continue to increase up to $\Omega_R \approx 1.3253$, where a saddle-node bifurcation (labeled as SN) is observed and it results in creation of stable large amplitude responses. The amplitude of this stable solution is increasing with a decrease of the shedding frequency and it is observed in the range of $\Omega_R \in (0.6665, 1.3253)$. As the frequency increases beyond $\Omega_R \approx 1.3253$, only trivial solution $a_1 = 0$ is found.

When β is decreased to 0.5, two branches of solutions occur as shown in Fig. 3(b). A large-amplitude solution is observed at a narrow range of low values of the nondimensional shedding frequency and a small-amplitude solution is found around main resonance frequency of $\Omega_R = 1$. For the large-amplitude solution, which has a similar varying trend as that of shown in Fig. 3(a), the Hopf and SN bifurcation occur at $\Omega_R \approx 0.2390$ and 0.3853 respectively. As the nondimensional shedding frequency increases, a pair of stable and unstable small-amplitude solutions is born via the SN bifurcation at $\Omega_R \approx 0.9690$. They exist over a small range of frequencies and disappear via the SN bifurcation at $\Omega_R \approx 1.2324$. Only trivial solution $a_1 = 0$ is observed in the range $\Omega_R \in (0.3853, 0.9690)$ and for the higher frequencies above $\Omega_R \approx 1.2324$.

For smaller values of the parameter β such as $\beta = 0.3$, only the small-amplitude solutions are found in the range of frequency near $\Omega_R = 1$ as shown in Fig. 3(c). As the parameter β is decreased further to 0.05, the similar scenario as that of for $\beta = 0.3$ is observed with the range of frequencies, where this pair of small amplitude solutions exist, is being reduced and lower values of amplitude are obtained. As β is decreased below 0.3, the occurrence of the first saddle node bifurcation is shifted to the higher values of the nondimensional shedding frequency while the second saddle node bifurcation is observed for lower values as can be seen from Figs 3(c) and 3(d).

Next the influence of the mass-damping parameter on the system responses was examined. Five sets of bifurcation curves for the amplitude ratio β varying between 0.8 and 0.05 were calculated for four different mass-damping parameters. Both amplitude of the structure response $a_1(\Omega_R)$ and wake oscillator amplitude $a_2(\Omega_R)$ were determined and they are presented in Figs 4 – 8 together with selected trajectories on the phase plane which were obtained by numerical integration of Eqs (12) and (13).

The results for $\beta = 0.8$ are shown in Fig. 4, where amplitudes $a_1(\Omega_R)$ and $a_2(\Omega_R)$ are presented in Figs. 4(a) and 4(b), respectively. Solid and dashed lines present the non-trivial analytical solutions of Eqs (54) and (55) and small circles demonstrate a direct numerical integration of Eqs (12) and (13) obtained for $\mu = 1, \xi = 0.003$. As can be seen from this figure, the same scenario as the one presented in Fig. 3(a) and described earlier is obtained for all considered mass-damping parameter

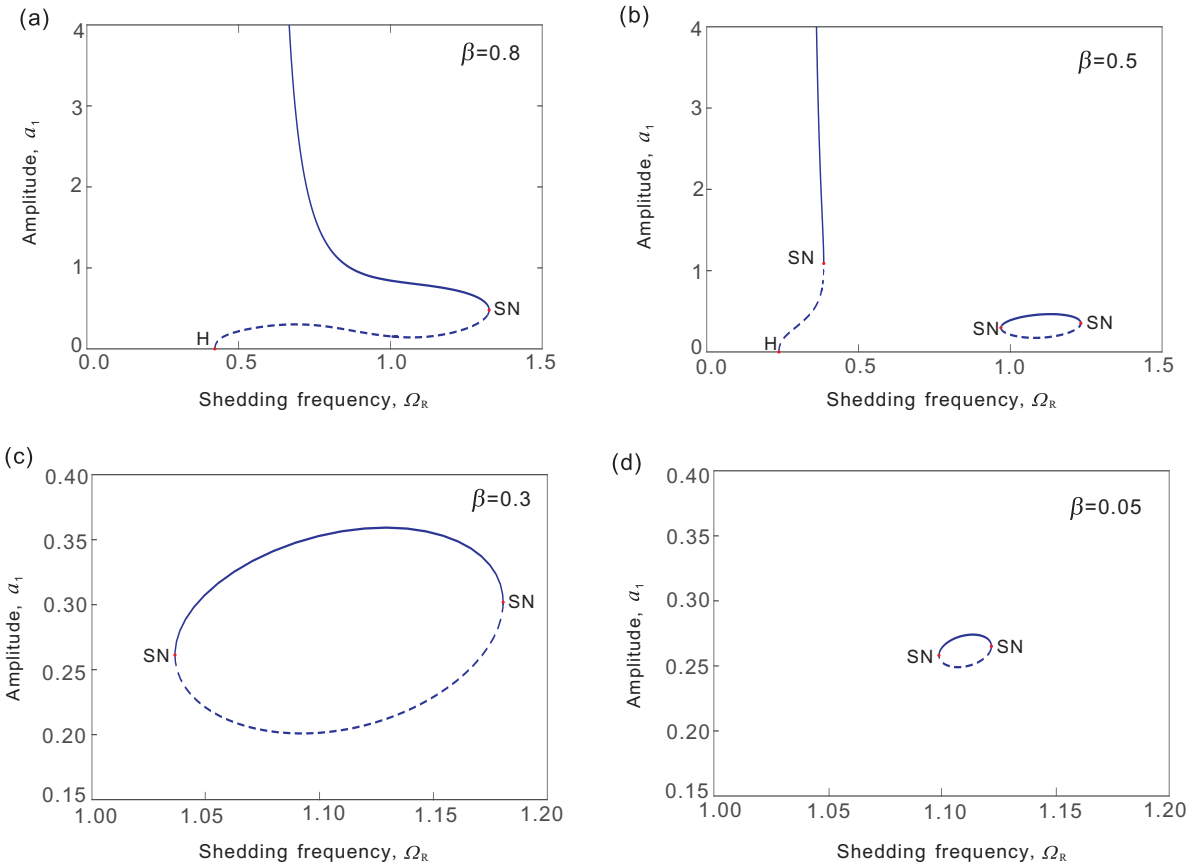

Fig. 3 Evolution of bifurcations of the amplitude-frequency curves for the structure obtained analytically (marked by solid and dashed curves) and numerically (marked by small circles) for different values of amplitude ratio β: (a) $\beta = 0.8$; (b) $\beta = 0.5$; (c) $\beta = 0.3$; (d) $\beta = 0.05$. As can be seen from the figures that the Hopf and SN bifurcation can occur under certain parameter conditions.

values. The large-amplitude oscillations are found in a relatively wide range of the nondimensional shedding frequency Ω_R and they undergo the Hopf and saddle-node bifurcations. With increasing the mass-damping parameters from $\mu = 1, \xi = 0.003$ to $\mu = 2.9, \xi = 0.045$, $\mu = 2.45, \xi = 0.00796$ and $\mu = 3.87, \xi = 0.0152$ successively, both Hopf and saddle-node bifurcations are observed for higher values of the nondimensional shedding frequency Ω_R. This is illustrated in Figs 4(a) and 4(b) by points $D_1(1.2, 0.7358)$, $E_1(1.2, 1.4875)$ and $D_2(1.2, 5.1159)$, $E_2(1.2, 6.3187)$, marked with the black solid circle.

Phase portraits of the original systems (12) and (13) are computed with Ω_R chosen at 1.2 for two values of mass-damping parameter – $\mu = 1, \xi = 0.003$ and $\mu = 2.9, \xi = 0.045$ and they are presented in Figs 4(c) and 4(d). Points in Figs 4(c) and 4(d) $D_1' = (0.7300, 0)$, $E_1' = (1.2781, 0)$ and $D_2' = (5.3661, 0)$, $E_2' = (6.2267, 0)$, show the evolution of the amplitudes on phase planes (panels (c) and (d) of Fig. 4) used to construct the frequency-amplitude curved (panels (a) and (b) of Fig. 4). As can be seen, the span of the system vibration is estimated well by the amplitudes obtained analytically.

Figure 5 presents the obtained results for $\beta = 0.7$. Here small circles in Fig. 5(a) and (b) demonstrate the results of numerical integrations of Eqs (12) and (13) obtained for $\mu = 3.87, \xi = 0.0152$. In general, the same behaviour is observed for this amplitude ratio value as for $\beta = 0.8$ described earlier. Phase portraits of the original systems (12) and (13) are computed for $\Omega_R = 1.1$ are presented in Figs 5(c) and 5(d) for all considered mass-damping parameter values, and very large-amplitude vibration are noticable for $\mu = 3.87$ and $\xi = 0.0152$.

As the amplitude ratio is decreased to $\beta = 0.5$, different bifurcation scenarios are observed as shown in Fig. 6. As can be seen from this figure for larger values of mass-damping parameter $\mu = 2.45, \xi = 0.00796$ (cyan curve) and $\mu = 3.87, \xi = 0.0152$ (black curve) the system response is similar to the case shown in Fig. 3(a) and also in Figs 4 and 5, while for smaller values of this parameter $\mu = 1, \xi = 0.003$ (blue curves) and $\mu = 2.9, \xi = 0.045$ (green curves), the

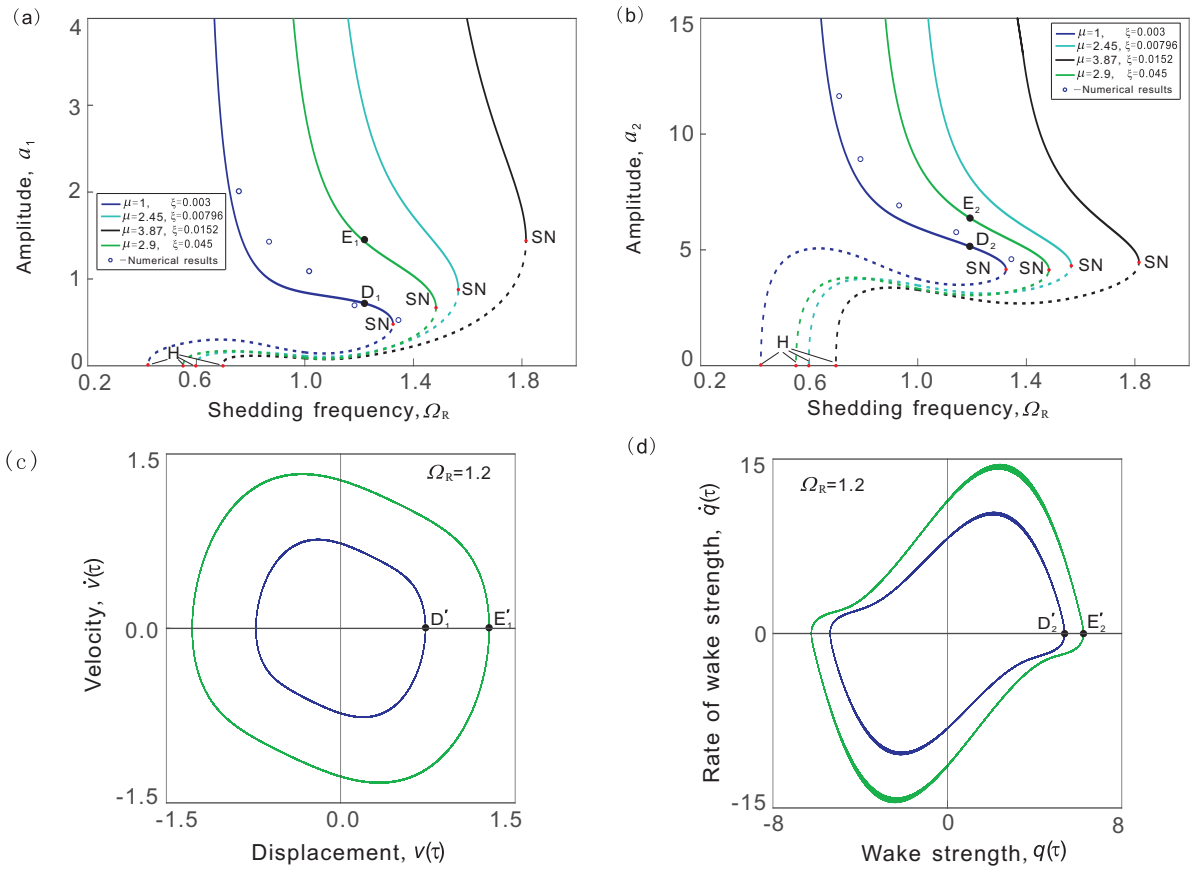

Fig. 4 (a) and (b) Bifurcations of the frequency-amplitude curves for the structure a_1 and the wake oscillator a_2 obtained analytically (marked by solid and dashed curves) and numerically (marked by small circles) for $\beta = 0.8$. The solid lines denote the stable solutions and the dashed lines denote the unstable solutions. Phase portraits of (c) the structure and (d) the wake oscillator computed for mass-damping parameters $\mu = 1, \xi = 0.003$ and $\mu = 2.9, \xi = 0.045$ at $\Omega_R = 1.2$.

behaviour is similar to the case shown in Fig. 3(b). In the case of larger mass-damping ratio where only one branch of solution exists, the Hopf bifurcations are observed at $\Omega_R = 0.3616$ for $\mu = 2.45, \xi = 0.00796$ and at $\Omega_R = 0.4418$ for $\mu = 3.87, \xi = 0.0152$, and the saddle node bifurcations occur at $\Omega_R = 1.3530$ for $\mu = 2.45, \xi = 0.00796$ and at $\Omega_R = 1.4524$ for $\mu = 3.87, \xi = 0.0152$. It should be noted that for a fixed nondimensional shedding frequency Ω_R, the amplitude for $\mu = 3.87, \xi = 0.0152$ is larger than that of for $\mu = 2.45, \xi = 0.00796$. In the case of smaller mass-damping ratio, where two branches of the solution exist, the unstable large amplitude solutions are born via Hopf bifurcation at $\Omega_R = 0.2390$ and they become stable at $\Omega_R = 0.3851$ for $\mu = 1, \xi = 0.003$ and at $\Omega_R = 0.2427, 0.3573$ respectively for $\mu = 2.9, \xi = 0.045$. A small amplitude solution branch is observed for $\Omega_R \in (0.9690, 1.2325)$ for $\mu = 1, \xi = 0.003$ and for $\Omega_R \in (0.9433, 1.2889)$ for $\mu = 2.9, \xi = 0.045$. In addition, Figs 6(c) and 6(d) present phase portraits of the original systems (12) and (13) computed for $\Omega_R = 1.1$. As can be seen from these figures, the amplitudes a_1 and a_2 are almost same for $\mu = 1, \xi = 0.003$ and $\mu = 2.9, \xi = 0.045$.

Fig. 7 presents the obtained results for $\beta = 0.3$. Here small circles in Fig.7(a) and 7(b) demonstrate the results of numerical integrations of Eqs (12) and (13) obtained for $\mu = 3.87, \xi = 0.0152$. As can be seen from this figure, the same scenario as the one presented in Fig. 3(c) and described earlier is obtained for all considered mass-damping parameter values. Only the small-amplitude responses are found in the range of frequency near $\Omega_R = 1$ and they appear and disappear through the saddle-node bifurcations. With increasing the mass-damping parameters from $\mu = 1, \xi = 0.003$ to $\mu = 2.9, \xi = 0.045$, $\mu = 2.45, \xi = 0.00796$ and $\mu = 3.87, \xi = 0.0152$ successively, the first saddle-node bifurcation is shifted to the lower values of the nondimensional shedding frequency while the second saddle node bifurcation is observed for higher values as can be seen from Fig. 7(a) and 7(b). Phase portraits of the original systems (12) and (13) computed for $\Omega_R = 1.15$ are presented in Figs 7(c) and 7(d) for all considered mass-damping parameter values, and when

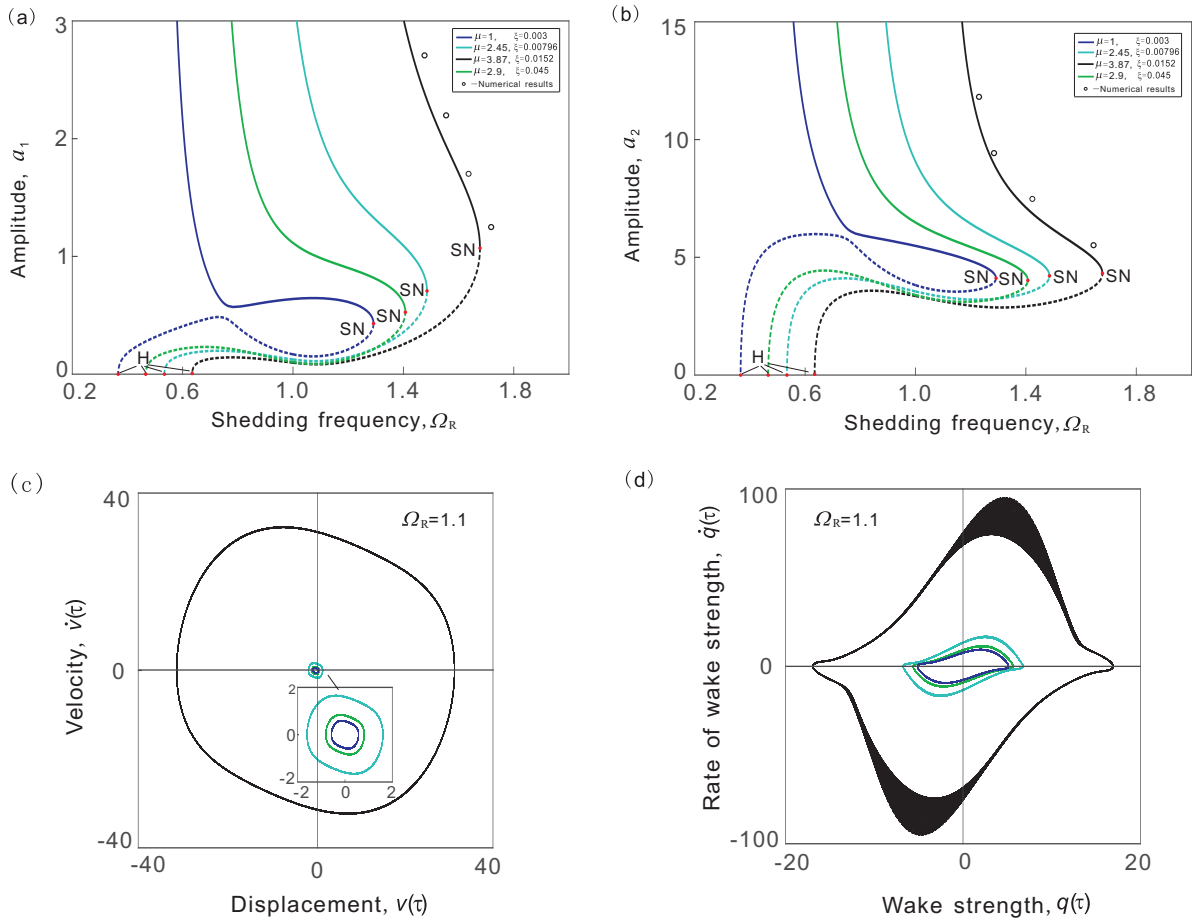

Fig. 5 (a) and (b) Bifurcations of the frequency-amplitude curves for the structure a_1 and the wake oscillator a_2 obtained analytically (marked by solid and dashed curves) and numerically (marked by small circles) for $\beta = 0.7$. The solid lines denote the stable solutions and the dashed lines denote the unstable solutions. Phase portraits of (c) the structure and (d) the wake oscillator computed for four values of mass-damping parameters at $\Omega_R = 1.1$.

$\Omega_R \in (1.0318, 1.0823)$, the amplitudes are very similar for $\mu = 2.45, \xi = 0.00796$ and $\mu = 3.87, \xi = 0.0152$, which are generated owing to the combination of mass-ratio and damping under the combined resonance condition.

Fig. 8 shows the obtained results for $\beta = 0.05$. Here small circles in Fig. 8(a) and (b) demonstrate the results of numerical integrations of Eqs (12) and (13) obtained for $\mu = 2.45, \xi = 0.00796$. The same behaviour is observed for this amplitude ratio value as for $\beta = 0.3$ described earlier but with the difference is the range of frequency as $\Omega_R \in (1.0989, 1.1219)$ for $\mu = 1, \xi = 0.003$, $\Omega_R \in (1.1042, 1.1305)$ for $\mu = 2.9, \xi = 0.045$, $\Omega_R \in (1.1231, 1.1572)$ for $\mu = 2.45, \xi = 0.00796$, and $\Omega_R \in (1.1339, 1.1734)$ for $\mu = 3.87, \xi = 0.0152$. Phase portraits of the original systems (12) and (13) computed for $\Omega_R = 1.1$ are presented in Figs 8(c) and 8(d) for $\Omega_R = 1.1$ when $\mu = 1$, $\xi = 0.003$ and $\mu = 2.9$, $\xi = 0.045$.

The presented results demonstrate that for small amplitude ratio β only small amplitude responses are found in the narrow range of nondimensional shedding frequency near $\Omega_R = 1$. As the amplitude ratio increases to $\beta = 0.5$, for lower mass-damping parameter values two branches of the solution are observed, i.e. similar small amplitude responses near $\Omega = 1$ and large amplitude responses at the lower nondimensional shedding frequencies. Finally as β increases from 0.5 to 0.8, two branches are merged together resulting in appearance of stable large amplitude solution over wide range of nondimensional shedding frequency for all considered values of mass-damping parameter.

6 Conclusions

A low dimensional model of a top tensioned riser (T-TR) under excitations from vortices and time-varying tension is investigated analytically by multiple scales method, where the van der Pol wake oscillator is used

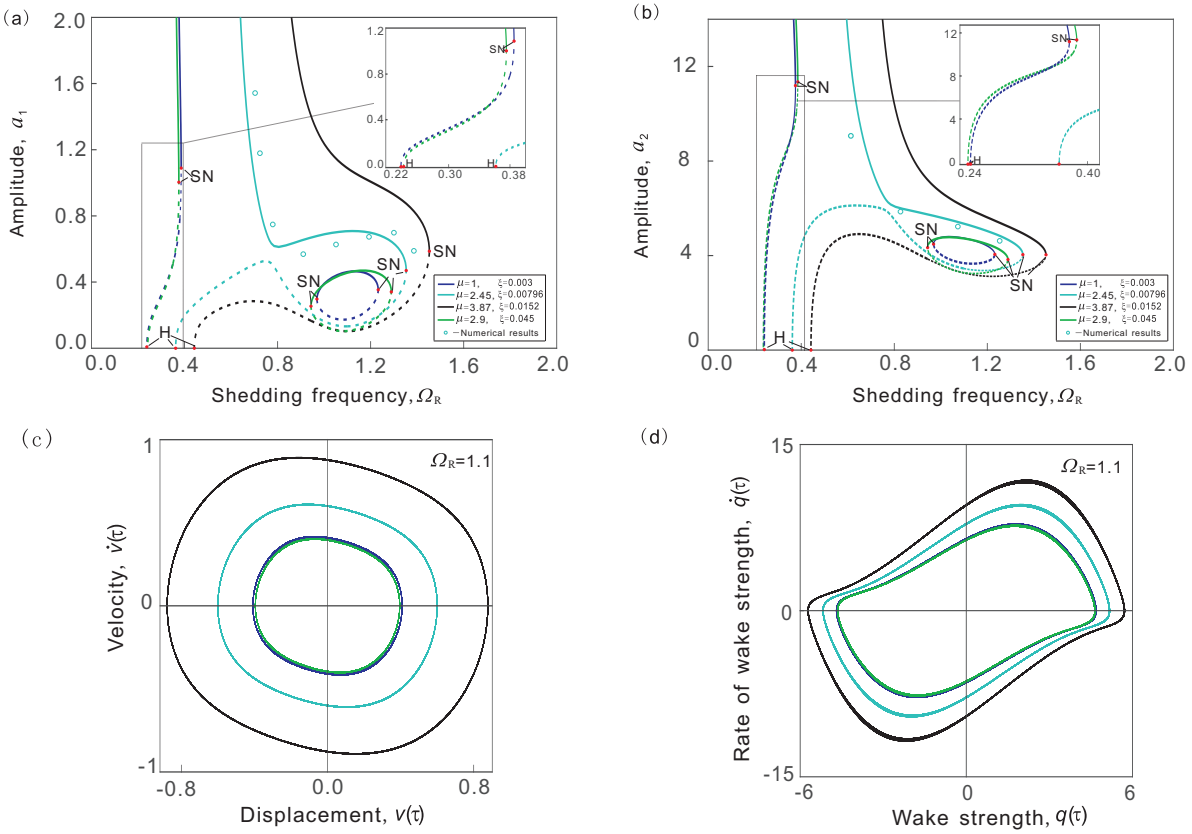

Fig. 6 (a) and (b) Bifurcations of the frequency-amplitude curves for the structure a_1 and the wake oscillator a_2 obtained analytically (marked by solid and dashed curves) and numerically (marked by small circles) for $\beta = 0.5$. The solid lines denote the stable solutions and the dashed lines denote the unstable solutions. Phase portraits of (c) the structure and (d) the wake oscillator computed for four values of mass-damping parameters at $\Omega_R = 1.1$.

to simulate the loading caused by the vortex shedding. The governing partial differential equations describing the fluid-structure interactions are formulated and multimode approximations are obtained using the Galerkin method. The one mode approximation is adopted in this study and two different system resonances are investigated employing the multiple scale method. They are the 1:1 internal resonance between the structure and wake oscillator (also known as 'lock-in' phenomenon) and the combined 1:1 internal and 1:2 parametric resonance.

Bifurcations of the system responses under the varying nondimensional shedding frequency for different mass-damping parameters are investigated and the results of multiple scale analysis are compared with numerical results obtained by the Runge-Kutta method. Analytical responses are calculated using the continuation method and their stability is determined by examining the eigenvalues of the corresponding characteristic equations. Influence of the system parameters including the amplitude of the tension variation, vortex shedding frequency and mass-damping parameter on the system bifurcations has been investigated.

First the 1:1 internal resonance between the structure and wake oscillator was studied. The amplitude-frequency equations were derived from the modulated equations, and bifurcation diagrams for the response amplitude under varying nondimensional shedding frequency were constructed for four different values of the mass-damping parameter. The presented results show that increasing the mass-damping parameter can suppress the oscillations of the structure and wake oscillator.

Then the combination of internal and parametric resonance was studied, where frequencies satisfy $\Omega_R \approx \omega_{R1}, \bar{\omega} \approx 2\omega_{R1}$. Here the influence of the amplitude ratio β on the dynamic responses was investigated and the results are presented for the same four values of the mass-damping parameter. A series of bifurcations including Hopf and saddle-node types were found analytically defining the range of existence of stable and unstable responses. The presented results demonstrate that for small amplitude ratio β only low amplitude responses are found in the narrow range of nondimensional shedding frequency near $\Omega_R = 1$. As the amplitude ratio increases to $\beta = 0.5$, for lower mass-damping param-

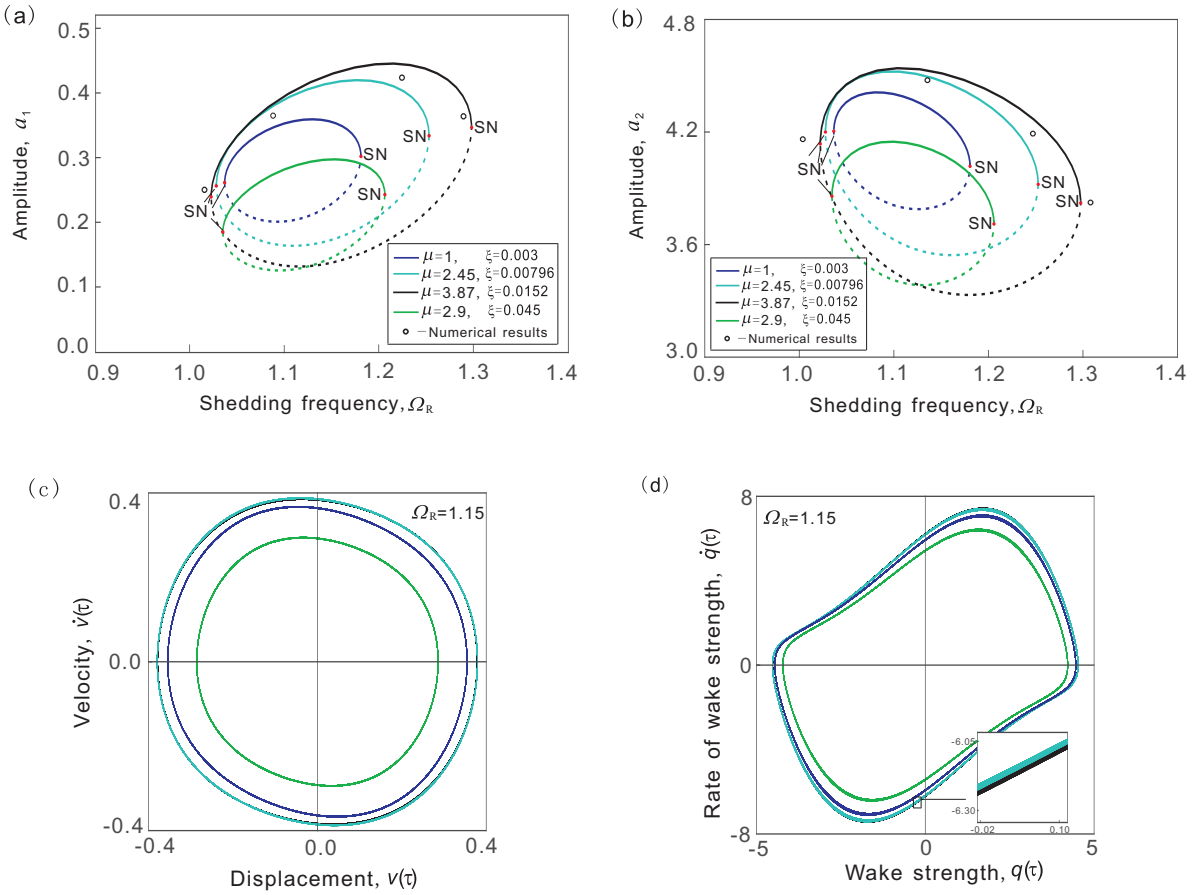

Fig. 7 (a) and (b) Bifurcations of the frequency-amplitude curves for the structure a_1 and the wake oscillator a_2 obtained analytically (marked by solid and dashed curves) and numerically (marked by small circles) for $\beta = 0.3$. The solid lines denote the stable solutions and the dashed lines denote the unstable solutions. Phase portraits of (c) the structure and (d) the wake oscillator computed for four values of mass-damping parameters at $\Omega_R = 1.15$.

eter values two branches of the solution are observed, i.e. similar small amplitude responses near $\Omega = 1$ and large amplitude responses at the lower nondimensional shedding frequencies. Finally as β increases from 0.5 to 0.8, two branches are merged together resulting in appearance of stable large amplitude solution over wide range of nondimensional shedding frequency for all considered values of mass-damping parameter.

In addition, results of analysis of the combined resonance comparing to that of only the internal resonance show that (i) amplitudes of responses of the structure under the combined resonance condition are much larger than that for the case of VIV only and the amplitude of responses increases rapidly as β grows; (ii) bifurcations including the saddle-node and Hopf bifurcations are observed in the considered frequency range; (iii) increasing the amplitude ratio β results in shift of the observed bifurcations to higher values of frequency Ω_R.

Acknowledgements The first two authors acknowledge the financial supports of the National Natural Science Foundation of China (No.11702111, 11732014), the Natural Science Foundation of Shandong Province (No. ZR2017QA005) and the State Scholarship Fund of CSC.

Declarations: The authors declare that they have no conflict of interest.

Data Availability Statements: The datasets generated during and/or analysed during the current study are available from the corresponding author on reasonable request.

References

1. Sarpkaya T. A critical review of the intrinsic nature of vortex-induced vibration. Journal of Fluids and Structures, 19, 389-447 (2004)
2. Williamson C.H.K., Govardhan R. Vortex-induced vibrations. Annual Review of Fluid Mechanics, 36, 413-455 (2004)
3. Williamson C.H.K., Govardhan R. A brief review of recent results in vortex-induced vibrations. Journal of Wind Engineering and Industrial Aerodynamics, 96, 713-735 (2008)
4. Hong K.-S., Shah U. H. Vortex-induced vibrations and control of marine risers: A review. Ocean Engineering 152, 300-315, (2018)

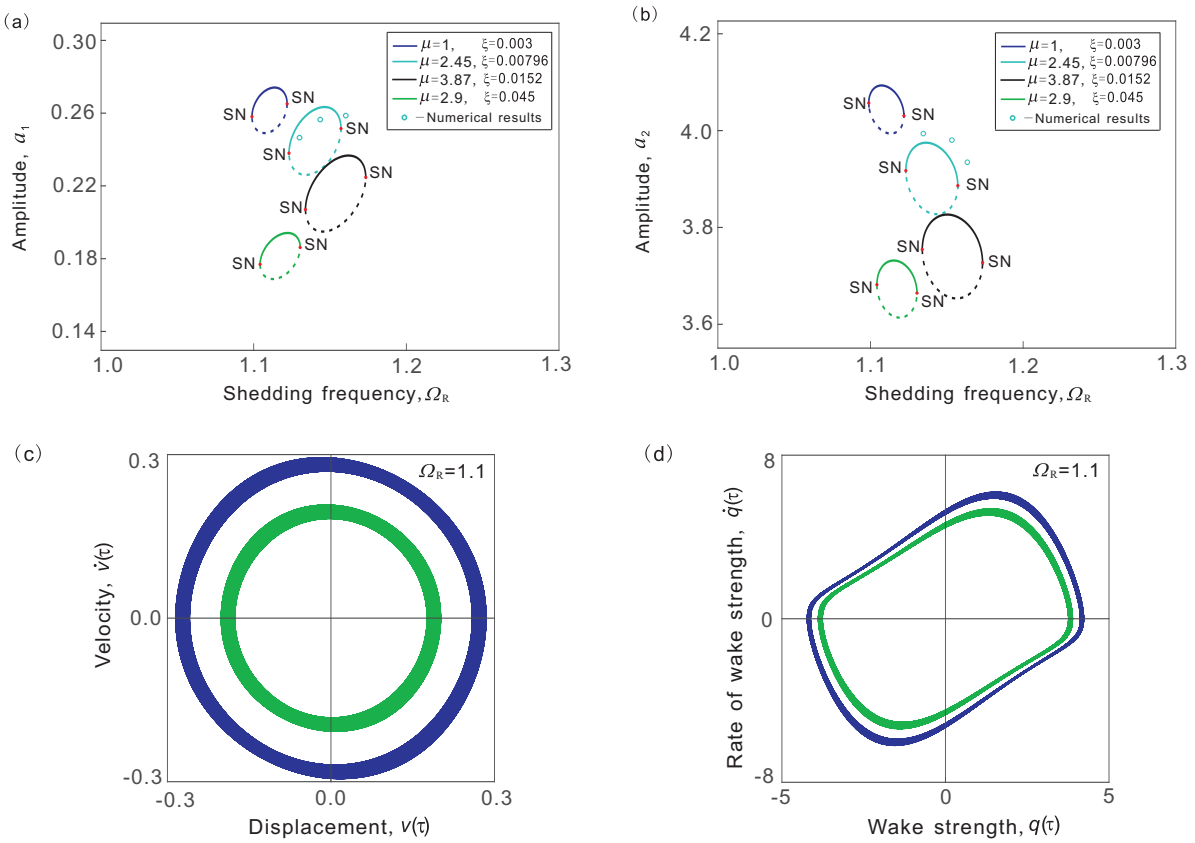

Fig. 8 (a) and (b) Bifurcations of the frequency-amplitude curves for the structure a_1 and the wake oscillator a_2 obtained analytically (marked by solid and dashed curves) and numerically (marked by small circles) for $\beta = 0.05$. The solid lines denote the stable solutions and the dashed lines denote the unstable solutions. Phase portraits of (c) the structure and (d) the wake oscillator computed for mass-damping parameters $\mu = 1, \xi = 0.003$ and $\mu = 2.9, \xi = 0.045$ at $\Omega_R = 1.1$.

5. Liu G., Li H., Qiu Z., Leng D., Li Z., Li W. Review: A mini review of recent progress on vortex-induced vibrations of marine risers. Ocean Engineering, 195, 1-17 (2020)
6. Jaiswal V., Vandiver J.K. VIV response prediction for long risers with variable damping. Proceedings of the 26th International Conference on Offshore Mechanics and Arctic Engineering, OMAE2007-29353, 1-9 (2007)
7. Morooka C.K., Tsukada R.I. Experiments with a steel catenary riser model in a towing tank. Applied Ocean Research 43, 244-255 (2013)
8. Franzini G.R., Gonçalves R.T., Pesce C.P., Fujarra A.L.C., Mazzilli C.E.N, Meneghini J.R., Mendes P. Vortex-induced vibration experiments with a long semi-immersed flexible cylinder under tension modulation: Fourier transform and Hilbert-Huang spectral analyses. Journal of the Brazilian Society of Mechanical Sciences and Engineering, 37, 589-599 (2015)
9. Mao L.J., Cai M.J., Yang Y.L., Wang G.R. Experimental study of the vortex-induced vibration of marine risers under middle flow. Journal of Vibroengineering, 20, 602-620 (2018)
10. Wang C.G., Cui Y.Y., Ge S.Q., Sun M.Y., Jia Z.R. Experimental study on vortex-induced vibration of risers considering the effects of different design parameters. Applied Sciences, 8, 1-19 (2018)
11. Zhu H., Gao Y., Zhao H. Coupling vibration response of a curved flexible riser under the combination of internal slug flow and external shear current. Journal of Fluids and Structures, 91, 1-32 (2019)
12. Chen W., Li M., Zheng Z., Tan T. Dynamic characteristics and VIV of deepwater riser with axially varying structural properties. Ocean Engineering, 42, 7-12 (2012)
13. Xue H. X., Wang K. P., Tang W. Y. A practical approach to predicting cross-flow and in-line VIV response for deepwater risers. Applied Ocean Research 52, 92-101 (2015)
14. Bourguet R., Triantafyllou M.S. Vortex-induced vibrations of a flexible cylinder at large inclination angle. Philosophical Transactions Royal Society A, 373, 1-19 (2015)
15. Tofa M.M., Maimun A., Ahmed Y.M. Effect of upstream cylinder's oscillation frequency on downstream cylinder's vortex indueced vibration. Proceedings of the ASME International Mechanical Engineering Congress and Exposition, 11-17 (2016)
16. Duan J., Chen K., You Y., Li J. Numerical investigation of vortex-induced vibration of a riser with internal flow. Applied Ocean Research, 72, 110-121 (2018)
17. Ulveseter J.V., Thorsen M.J., Sævik S., Larsen C.M. Simulating fundamental and higher harmonic VIV of slender structures. Applied Ocean Research, 90, 1-16 (2019)
18. Xue H.X., Yuan Y.C., Tang W.Y. Numerical investigation on vortex-induced vibration response characteristics for flexible risers under sheared-oscillatory flows. International Journal of Naval Architecture and Ocean Engineering, 11, 923-938 (2019)
19. Li X.M., Wei W.F., Bai F.T. A full three-dimensional vortex-induced vibration prediction model for top-tensioned risers based on vector form intrinsic finite element method. Ocean Engineering 218, 1-18 (2020)

20. Sanaati B., Kato N. Vortex-induced vibration (VIV) dynamics of a tensioned flexible cylinder subjected to uniform cross-flow. Journal of Marine Science and Technology, 18, 247-261 (2013)
21. Chen W., Zhang Q., Li H., Hu H. An experimental investigation on vortex induced vibration of a flexible inclined cable under a shear flow. Journal of Fluids and Structures, 54, 297-311 (2015)
22. Hu Z., Wang J., Sun Y. Flow-induced vibration of one-fixed-one-free tandem arrangement cylinders with different mass-damping ratios using wind tunnel experiment. Journal of Fluids and Structures, 96, 1-25 (2020)
23. Tsahalis D. T., Jones W. T. Vortex-induced vibrations of a flexible cylinder near a plane boundary in steady flow. Offshore Technology Conference, Houston, Texas (1981)
24. Yang B., Gao F., Jeng D., Wu Y. Experimental study of vortex-induced vibrations of a cylinder near a rigid plane boundary in steady flow. Acta Mechanica Sinica, 25, 51-63 (2009)
25. He C.J., Duan Z.D., Ou J.P. Numerical simulation of self-excited and forced vibration of circular cylinders in current. China Ocean Engineering, 24, 135-144 (2010)
26. Sun L., Liu C.F., Zong Z., Dong X.L. Fatigue damage analysis of the deepwater riser from VIV using pseudo-excitation method. Marine Structures, 37, 86-110 (2014)
27. Fu B.W., Duan M.Y., Wan D.C. Effect of mass ratio on the vortex-induced vibrations of a top tensioned riser. The Second Conference of Global Chinese Scholars on Hydrodynamics, Wuxi, China, Nov. (2016)
28. Song L., Fu S., Cao J., Ma L., Wu J. An investigation into the hydrodynamics of a flexible riser undergoing vortex-induced vibration. Journal of Fluids and Structures, 63, 325-350 (2016)
29. Konstantinidis E., Zhao J., Leontini J., Jacono D. L., Sheridan J. Phase dynamics of effective drag and lift components in vortex-induced vibration at low mass–damping. Journal of Fluids and Structures, 96, 1-26 (2020)
30. Facchinetti M.L., de Langrea E., Biolley F. Coupling of structure and wake oscillators in vortex-induced vibration. Journal of Fluids and Structures, 19, 123-140 (2004)
31. Zanganeh H., Srinil N. Three-dimensional VIV prediction model for a long flexible cylinder with axial dynamics and mean drag magnifications. Journal of Fluids and Structures, 66, 127-146 (2016)
32. Postnikov A., Pavlovskaia E., Wiercigroch M. 2DOF CFD calibrated wake oscillator model to investigate vortex-induced vibrations. International Journal of Mechanical Sciences, 127, 176-90 (2017)
33. Kurushina V., Pavlovskaia E., Postnikov A., Wiercigroch M. Calibration and comparison of VIV wake oscillator models for low mass ratio structures. International Journal of Mechanical Sciences, 142-143, 547-560 (2018)
34. Kurushina V., Pavlovskaia E., Wiercigroch M. VIV of flexible structures in 2D uniform flow. International Journal of Engineering Science, 150, 1-24 (2020)
35. Pavlovskaia E., Keber M., Postnikov A., Reddington K., Wiercigroch M. Multi-modes approach to modelling of vortex-induced vibration. International Journal of Non-Linear Mechanics, 80, 40-51, (2016)
36. Ogink R.H.M., Metrikine A.V. A wake oscillator with frequency dependent coupling for the modeling of vortex-induced vibration. Journal of Sound and Vibration, 329, 5452-5473 (2010)
37. Qu Y., Metrikine A.V. A wake oscillator model with nonlinear coupling for the vortex-induced vibration of a rigid cylinder constrained to vibrate in the cross-flow direction. Journal of Sound and Vibration, 469, 1-26, (2020)
38. Hsu C.S. The response of a parametrically excited hanging string in fluid. Journal of Sound and Vibration, 39, 305-316 (1975)
39. Chatjigeorgiou I.K., Mavrakos S.A. Bounded and unbounded coupled transverse response of parametrically excited vertical marine risers and tensioned cable legs for marine applications. Applied Ocean Research, 24, 341-354 (2002)
40. Chatjigeorgiou I. K., Mavrakos S.A. Nonlinear resonances of parametrically excited risers – numerical and analytic investigation for $\Omega = 2\omega_1$. Computers and Structures, 83, 560-573 (2005)
41. Zhang J., Guo H., Tang Y., Li Y. Effect of top tension on vortex-induced vibration of deep-sea risers. Journal of Marine Science and Engineering, 8, 1-14 (2020)
42. Li P., Cong A., Dong Z., Wang Y., Liu Y., Guo H., Li X., Fu Q. Investigation on vortex-induced vibration experiment of a standing variable-Tension deepsea riser based on BFBG sensor technology. Sensors, 19, 1-19 (2019)
43. Srinil N. Analysis and prediction of vortex-induced vibrations of variable-tension vertical risers in linearly sheared currents. Applied Ocean Research, 33, 41-53 (2011)
44. Yang H., Xiao F. Instability analyses of a top-tensioned riser under combined vortex and multi-frequency parametric excitations. Ocean Engineering, 81, 12-28 (2014)
45. Yang H., Xiao F., Xu P. Parametric instability prediction in a top-tensioned riser in irregular waves. Ocean Engineering, 70, 39-50 (2013)
46. Wang Y., Gao D., Fang J. Coupled dynamic analysis of deepwater drilling riser under combined forcing and parametric excitation. Journal of Natural Gas Science and Engineering, 27, 1739-1747 (2015)
47. Thorsen M.J., Sævik S. Vortex-induced vibrations of a vertical riser with time-varying tension. Procedia Engineering, 199, 1326-1331 (2017)
48. Fu B., Wan D. Numerical study of vibrations of a vertical tension riser excited at the top end. Journal of Ocean Engineering and Science, 2, 268-278 (2017)
49. Yuan Y., Xue H., Tang W. A numerical investigation of vortex-induced vibration response characteristics for long flexible cylinders with time-varying axial tension. Journal of Fluids and Structures, 77, 36-57 (2018)
50. Zhang X., Gou R., Yang W., Chang X. Vortex-induced vibration dynamics of a flexible fluid-conveying marine riser subjected to axial harmonic tension. Journal of the Brazilian Society of Mechanical Sciences and Engineering, 40, 1-12 (2018)
51. Lou M., Hu P., Qi X., Li H. Stability analysis of deepwater compliant vertical access riser about parametric excitation. International Journal of Naval Architecture and Ocean Engineering, 11, 688-698 (2019)
52. Wu Z., Xie C., Mei G., Dong H. Dynamic analysis of parametrically excited marine riser under simultaneous stochastic waves and vortex. Advances in Structural Engineering, 22, 268-283 (2019)
53. Gao G., Cui Y., Qiu X. Prediction of vortex-induced vibration response of deep sea top-tensioned riser in sheared flow considering parameteric exicitations. Polish Maritime Research, 2, 48-57 (2020)
54. Zhu H., Geng G., Yu Y., Xu L. Probabilistic analysis on parametric random vibration of a marine riser excited by correlated Gaussian white noises. International Journal of Non-Linear Mechanics, 126, 1-10 (2020)
55. Guijie Liu, Haiyang Li, Zhaozun Qiu, Zhixiong Li. A comprehensive numerical analysis of cross-flow vortex-induced vibrations for top tension risers under different flows. Physics of Fluids, 32, 1-21, (2020).

56. Koska R., Kaculi J., Campbell M., Mills D. Minimizing interference between top tension risers for tension leg platforms. Proceedings of the ASME, 32nd International Conference on Ocean, Offshore and Arctic Engineering, France (2013)
57. Keber M., Wiercigroch M. Dynamics of a vertical riser with weak structural nonlinearity excited by wakes. Journal of Sound and Vibration, 315(3), 685-699 (2008)
58. Keber M. Vortex induced vibration of offshore risers: theoretical modelling and analysis. PhD thesis, Aberdeen (2012)
59. Wang D., Chen Y., Wiercigroch M., Cao Q. A three-degree-of-freedom model for vortex-induced vibrations of turbine blades. Meccanica, 51, 2607-2628 (2016)
60. Wang D., Chen Y., Wiercigroch M., Cao Q. Bifurcation and dynamic response analysis of rotating blade excited by upstream vortices. Applied Mathematics and Mechanics (English Edition), 37, 1251-1274 (2016)
61. Clough R. W., Penzien J. Dynamics of structures. Computers and Structures, Inc., 3rd edition, (2003)
62. Keber M., Wiercigroch M. A reduced order model for vortex-induced vibration of a vertical offshore riser in lock-in. IUTAM symposium on fluid-structure interaction in Ocean engineering, Iutam Bookseries Volume, 8, 155-166 (2008)
63. Nayfeh A. H., Mook D. T. *Nonlinear oscillations*. New York (1979)
64. Nayfeh A. H. Resolving controversies in the application of the method of multiple scales and the generalized method of averaging. Nonlinear Dynamics, 40(1), 61-102 (2005)
65. Schmidt G., Tondl A. *Nonlinear vibration*. Cambrige: Cambrige University Press. (1986)